Molecular beam measurements of inelastic cross sections for transitions between defined rotational states (j,m) of CsF in collisions with He, Ne, Ar, Kr, CH4, CF4, SF6, C2H6, N2, CO, CO2, N2O, CH3Cl, CH3Br, CF3H, and CF3Br

U. Borkenhagen, H. Malthan, and J. Peter Toennies

Articles you may be interested in

Photoemission cross sections for CH radicals produced by collisions of He (2 3 S) atoms with CH 3 X (X=H, Cl, Br, I)
J. Chem. Phys. **106**, 4491 (1997); 10.1063/1.473493

Refractivity virial coefficients of gaseous CH4, C2H4, C2H6, CO2, SF6, H2, N2, He, and Ar
J. Chem. Phys. **94**, 5669 (1991); 10.1063/1.460478

Excitation cross sections in collisions of He+, Ne+, Ar+, N+, N+ 2, O+ 2, H+ 2, and H+ 3 ions with CF4
J. Chem. Phys. **86**, 1938 (1987); 10.1063/1.452143

Photoabsorption cross sections of CH4, CF4, CF3Cl, SF6, and C2F6 from 175 to 770 Å
J. Chem. Phys. **67**, 1237 (1977); 10.1063/1.434935

Diffusivity of 3He, 4He, H2, D2, Ne, CH4, Ar, Kr, and CF4 in (C4F9)3N
J. Chem. Phys. **55**, 4715 (1971); 10.1063/1.1675569

Molecular beam measurements of inelastic cross sections for transitions between defined rotational states (j,m) of CsF in collisions with He, Ne, Ar, Kr, Xe, CH$_4$, CF$_4$, SF$_6$, C$_2$H$_6$, N$_2$, CO, CO$_2$, N$_2$O, CH$_3$Cl, CH$_3$Br, CF$_3$H, and CF$_3$Br

U. Borkenhagen,[a] H. Malthan,[b] and J. Peter Toennies

Max-Planck-Institut für Strömungsforschung, 3400 Göttingen, Federal Republic of Germany

Absolute inelastic cross sections for rotational quantum state to state transitions have been measured in small angle grazing collisions of CsF molecules in collisions with He, Ne, Ar, Kr, Xe, CH$_4$, CF$_4$, SF$_6$, C$_2$H$_6$, N$_2$, CO, CO$_2$, N$_2$O, CH$_3$Cl, CH$_3$Br, CF$_3$H, CH$_3$Cl, CF$_3$Br. For the rare gas collision partners the following $\Delta j = 1$, $\Delta m = 0$ transitions were measured: (j,m) = (1,0)→(2,0), (2,0)→(1,0), (2,0)→(3,0), (3,0)→(2,0) as well as the $\Delta j = 2$, $\Delta m = 0$ transition (3,0)→(1,0). In addition the $\Delta j = 1$, $\Delta m = 1$ transitions (1,1)→(2,0) and (2,0)→(3,1) and the pure $\Delta m = 1$ transitions (1,1)→(1,0) and (3,0)→(3,1) were measured. In each case the signs of m and Δm are undetermined. For the other scattering partners only the $\Delta j = 1$, $\Delta m = 0$ and $\Delta j = 2$, $\Delta m = 0$ transitions were measured. In the collision region the quantization axis of the CsF molecules is defined by a weak electric field (300 V/cm) directed perpendicular to the direction of the velocity selected CsF and the target nozzle beam and thus perpendicular to the relative velocity vector. The apparatus and the techniques used to determine the absolute cross sections are given and the formulas used to derive the various types of cross sections from the pressure dependences are derived. Because of the favorable geometry and nearly monoenergetic conditions it was possible to calculate by a Monte Carlo method a transmission function for each rare gas and transition studied. The tabulated transmission functions make it possible to compare theoretical predicted differential cross sections directly with the reported values. An approximate analytic expression is also given for the (2,0)→(3,0) transition which can be used for all scattering targets. This approximate transmission function is then used to obtain absolute cross sections in the center of mass system for all systems. These cross sections are correlated with the predictions of a Born-approximation theory for the various predominant potential terms. The correlation shows that for the first 8 partners the induced dipole–quadrupole induction term is predominant. For the molecules C$_2$H$_6$, N$_2$, CO, CO$_2$ and N$_2$O an electrostatic dipole–quadrupole potential is dominant, while for the polar symmetric top molecules the dipole–dipole potential is producing the transitions. The results suggest that the method can be used to determine quadrupole moments.

I. INTRODUCTION

The inelastic cross sections for rotational transitions are the simplest of a large class of energy transfer collision processes which are of fundamental importance for gas kinetics.[1] The recent development of gas lasers, laser isotope separation techniques as well as the observation of the microwave spectra of interstellar molecules have all pointed to a need for detailed knowledge of these cross sections. Although methods are now available for computing inelastic cross sections and the corresponding rate constants,[1] the results depend sensitively on the exact shape of the intermolecular potential which is only known with sufficient accuracy for a few systems.[1] Since theory is still not able to predict the potentials with sufficient accuracy we have to rely on experimental data. The bulk methods used in the past now appear to be relatively insensitive to the important potential features. Molecular beam scattering experiments[2] of two fundamentally different types have on the other hand been shown to be very useful for probing the radial dependence of the potential anisotropy which is largely responsible for rotational transitions. In the

one technique the total integral cross sections of polarized molecular beams are measured for two orientations with respect to the collision directions.[3] In the other technique the inelastic cross section is measured; usually by an energy loss technique.[2] With this latter technique it has so far only been possible to resolve the rotational quantum transitions of hydrogen molecules.[4] Unfortunately, the narrow spacing of the rotational levels of heavier molecules makes the resolution of individual state to state transitions with this technique very difficult and results are only available for unresolved energy loss distributions.[5]

The use of electrostatic quadrupole deflection fields makes it possible to measure inelastic cross sections for collision induced rotational transitions of polar alkali-halide molecules MX in well defined rotational states (j, m), where j and m are the rotational and magnetic quantum numbers (the sign of m is undetermined):

$$\text{MX}(j_i, m_i) + \text{A} \rightarrow \text{MX}(j_f, m_f) + \text{A}$$
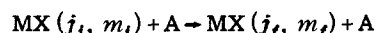
where A is a rare gas atom, a diatomic or a polyatomic molecule. The transitions are identified by the change in the effective electric dipole moment of the primary beam molecule undergoing transition. Since molecules with different $|m|$-states are selected, the molecules can be polarized in an electric field E in the scattering

[a] Friederichshöh 9, -2361- Todesfelde.
[b] IABG, Industrie-Anlagen-Betriebsgesellschaft, Einstein-Str. -8012- Ottobrunn b. München.
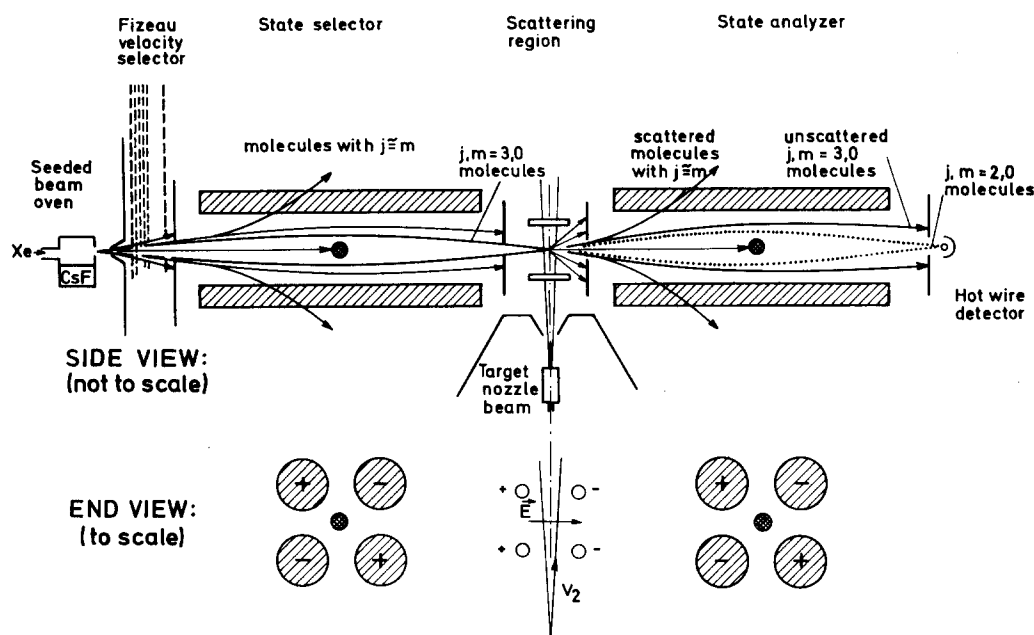
FIG. 1. State selection apparatus used to measure the integral over small scattering angles of the differential inelastic cross section for the collision induced transition $(j, m) = (3, 0) \rightarrow (2, 0)$. The alkali–halide molecules are rotationally cooled in a Xe nozzle beam, velocity selected and then state selected by the first electrostatic quadrupole field. The beam stops and apertures permit only molecules in the $(3, 0)$ state to pass into the scattering region. Here they are polarized by an electric field E produced by four wires. E is perpendicular to the secondary and primary beam direction and thus the relative velocity is always perpendicular to the polarization direction. Buffer fields (not shown) prevent randomization of the m states as the molecules pass in and out of the scattering region. Of the molecules entering the state analyzer only the inelastically scattered $(2, 0)$ molecules are able to arrive at the hot wire detector. In the figure the vertical dimensions are vastly exagerated compared to the longitudinal dimensions.

region and collisions with a well defined direction of the relative velocity g, with respect to E can be studied. Furthermore since the deflection in the inhomogeneous electric quadrupole field depends on the field induced effective dipole moment, which is inversely proportional to the rotational energy constant, this technique can be used to study transitions between the closely spaced rotational levels of heavy polar molecules.

In the first experiments of this type the $(j, m) = (2, 0)$ $\rightarrow (3, 0)$ transitions of TlF in small angle scattering from He, Ne, Ar, Kr, CH_4, SF_6, H_2, O_2, N_2O, H_2O, and CF_2Cl_2 were observed.[6] Small angle collisions were studied since these can be analyzed using a semiclassical theory in which a straight line trajectory is used and the transition probability is calculated from the Born approximation.[7] Since the target gas was in a scattering chamber, the interpretation of the results was made difficult by the averaging over the broad distributions of both the magnitude and direction of the relative velocities g. More recently these early experiments were repeated by Borkenhagen et al.[8] $(j, m = 2, 0 \rightarrow 3, 0)$ and Henrichs et al.[9] $(j, m = 2, 0 \rightarrow 1, 0)$ using CsF instead of TlF. The interpretation of both experiments is much more direct than in the original experiments since a target nozzle beam with a narrow velocity distribution was used. The results of Borkenhagen et al. are in surprisingly good agreement with the early experiments. In this paper we report on a more extensive study of nine different transitions involving the $(j, m) = (1, 0)$, $(1, 1)$, $(2, 0)$, $(3, 0)$, and $(3, 1)$ states of CsF in collisions with He, Ne, Ar, Kr, Xe, and four transitions of CsF in collisions with CH_4, CF_4,

SF_6, C_2H_6, N_2, CO, CO_2, N_2O, CH_3Cl, CH_3Br, CF_3H, CF_3Cl, and CF_3Br.[10]

After a brief description of the principle of the apparatus and measuring method the apparatus and its important properties are fully described. The method used to extract cross sections from the measured intensities is discussed in detail. The results are then presented in tabular form. The next section shows how it is possible to relate the measured cross sections to differential cross sections in the center of mass system. In the final section the results are compared with previous work and discussed in terms of the dominant interaction terms.

II. APPARATUS

Figure 1 shows a schematic diagram of the apparatus. A Xe seeded CsF nozzle beam is velocity selected and collimated before entering the first electrostatic quadrupole. The voltage is set such that only molecules in one given rotational state [e.g., $(j, m = (3, 0)$] can pass the small exit slit and enter the scattering region. The state selected beam then passes adiabatically (to avoid Δm transitions) into the scattering region where it is crossed at 90° by a target nozzle beam. The molecules are oriented by a nearly homogeneous electric field E perpendicular to both the velocity vector of the MX beam v_{MX} and that of the target beam v_A. Thus the relative velocity g is always perpendicular to E. Molecules scattered through small angles ($\leq 2°$ in the center of mass (CM) system) pass adiabatically into the analyzer

TABLE I. Important dimensions (all values in mm).

Longitudinal distances		Transverse distances	
Nozzle-skimmer	10–30 variable		
Skimmer length	25	Skimmer diameter	0.38
Skimmer angle	25°/32°		
Skimmer base—adjustable aperture	140	Aperture diameter	2 (A) 1 (B)
Adjustable aperture— state selector quadrupole	15		
Length of state selector	910	Diagonal distance between rods	8.6
Distance to obstacle	508	Obstacle diameter	2
State selector quadrupole— guide field	5		
Length of guide field	65	Guide field rod diameter	7
		Diagonal distance between rods	7
Guide field—orientation field	5	Entrance aperture diameter[a]	1
Length of orientation field	70	Orientation field wire diameter	0.4
		Diagonal distance between wires	14
Orientation field—guide field	5	Exit aperture diameter[b]	8
Length of guide field	65	Guide field rod diameter	7
Guide field–state analyzer	5		
Length of state analyzer	829	Diagonal distance between rods	8.6
Distance to obstacle	403	Obstacle diameter	2
State analyzer (end)— detector ribbon	104	Effective detector area	0.7 ± 0.4

[a]Mounted at the beginning of the orientation field.
[b]Mounted at the end of the orientation field.

quadrupole which focusses only molecules in a specified rotational state on to the detector.

Details of the apparatus are described in two reports.[10] Here we discuss only the important properties of the components and the slit geometry and dimensions. The vacuum system is divided into the following chambers with the corresponding effective pumping speeds and operating pressures: oven chamber: 3000 l/s, 10^{-4} Torr; velocity selector chamber: 500 l/s, 2×10^{-5} Torr; state selector chamber: 700 l/s, 4×10^{-6} Torr; scattering chamber: 3600 l/s, 3×10^{-7} Torr; target nozzle beam chamber: 6000 l/s, 2×10^{-5} Torr; state analyzer chamber: 700 l/s, 5×10^{-6} Torr.

The primary beam source is a conventional two chamber inconel oven. The oven was filled with CsF (99.9% pure) and operated at a temperature between 800 and 1000 K ($P_{CsF} \simeq 1.4 \times 10^{-2}$ to 1.42 Torr). Xe (99.9% pure) was passed into the main chamber through a heated (to prevent condensation and clogging) narrow bore tube. The inlet pressure measured (outside the oven) was between 500 and 1500 Torr and the pressure in the oven was estimated to be somewhat less. The oven hole was 0.5 mm in diameter. A long (25 mm) slender (25°/32°)

0.4 mm diameter skimmer was mounted at a (variable) distance of about 20 mm from the oven.

Two conventional rotating disc velocity selectors were used. One had a nominal resolving power of $\Delta v/v = 5.8\%$ (fwhm) and a nominal transmission of 38%. Another selector using photoetched discs (20 cm diameter 1540 slits 0.2 mm width separated by teeth of 0.2 mm width) was used to achieve a higher nominal velocity resolution $\Delta v/v = 2.9\%$ in some of the runs. The beam divergence was defined by a 1 mm diameter adjustable aperture mounted between the velocity and state selector. An 8 mm long 2 mm diameter channel served to isolate the vacuum in the velocity selector chamber from the state selector chamber. Table I lists the locations and sizes of the beam defining circular apertures and obstacles.

The quadrupole fields were approximated by using 4 cylindrical stainless rods of 10 mm diameter. The distance between the surfaces of diagonally opposite rods was 8.6 mm. The rods were carefully adjusted and the largest deviation in the ideal relative positions was less than 0.03 mm. At roughly the middle of each quadrupole (see Table I) a gap of 8 mm was introduced to permit in-
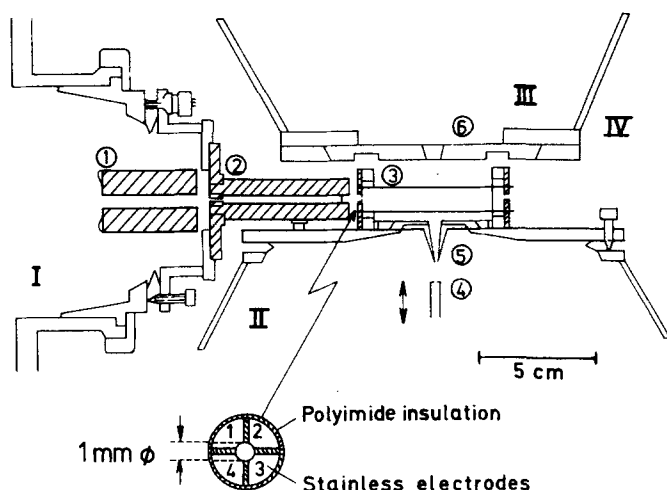
FIG. 2. Roughly to scale sideview of the scattering chamber. The numerals I, II, III, and IV designate parts of separately pumped chambers. The primary beam enters the scattering region from the left. After leaving the state selector quadrupole (1) it passes by way of a buffer guide field (2) into the scattering region through a 1 mm entrance aperture with electrodes on each quadrant (see insert). Here a nearly homogeneous electric field is formed by four wires (3). The target nozzle beam (4) is collimated by a skimmer (5) and passes upwards into the sump vacuum stage III through the aperture (6). After scattering the primary beam passes through an exit aperture (8 mm dia.) and an identical buffer guide field to the right into the state analyzer and on to the detector.

sertion of a metal spherical obstacle which was 2 mm diameter and could be adjusted from the outside to 0.01 mm.

The scattering chamber is shown in more detail in Fig. 2. After leaving the selector quadrupole the beam passes through a 65 mm long buffer field (4 cylindrical rods, 7 mm diameter and 7 mm diagonal distance) before entering the scattering region through a 1 mm diameter aperture which was made up of four electrically isolated (with separate voltage supplies) stainless quadrants (see Fig. 2). An optimal field on these quadrants served to reduce undesirable Δm transitions. The method used to identify Δm transitions is discussed in the next section. In the scattering region a nearly homogeneous field was maintained by 4 (0.4 mm diameter) wires. The two at the back and two at the front each had a voltage of $+150$ V and -150 V, respectively and the homogeneous field strength was estimated to be $\simeq 300$ V/cm. As noted earlier[3(a),6(b)] it was necessary to heat each of the wires continuously during the measurements to reduce surface charging and achieve a high degree of polarization. The buffer field at the state analyzer end of the scattering region was identical to that just described. The target nozzle beam was operated at pressures between 150 and 1200 Torr. The nozzle (0.05 mm diameter) was 8 mm from the 15 mm long slender (25/32°) skimmer with 0.65 mm diameter opening.

The quadrupole state analyzer had the same rod dimensions as the polarizer, but was somewhat shorter: 828 mm instead of 910 mm.

The detector was a hot wire surface ionization detector with a homemade quadrupole mass filter followed by a multiplier (EMI Type 9643/2B). For details on the detector see also Refs. 3a and 6b. The individual ions were counted and the count rates were stored in a minicomputer (NOVA 1200) via a CAMAC crate system. The entire apparatus was controlled by the computer to make possible an uninterrupted series of measurements over a period of one or two weeks.

Two different apparatus configurations with different rotational state resolution in the A field were used in the measurements. In the configuration A (low resolution) the nominal resolution of the rotor was 5.8% and the aperture between skimmer and state selector quadrupole was 2 mm diameter. The oven was operated at 800 K and the velocity selector was set at 480 m/s. In the configuration B (high resolution) the nominal resolution of the rotor was 2.9% and the aperture was 1 mm diameter and the oven was hotter (1000 K) to compensate for the loss of intensity. The velocity selector was set at 550 m/s.

III. EXPERIMENTAL DETAILS[11]

A. The nozzle beam source

The use of a Xe seeded nozzle beam source[12] leads to a cooling of both the translational as well as the rotational degrees of freedom of CsF to about 6 K.[14] The translational cooling meant that the fraction of the state-selected beam, transmitted by the velocity selector, increased from about 2.3% ($P_{Xe} = 0$ Torr) to 15% ($P_{Xe} \gtrsim 600$ Torr). In addition, the rotational cooling leads to an intensity enhancement, which is estimated directly from the Boltzmann distribution. For $B \ll kT$ ($B_{CsF}/k = 0.265$ K) the fraction X of the total population in one rotational state can be approximated by

$$X(j, T) \simeq B/kT . \tag{1}$$

B. State selection

Figure 3 shows the focussing properties of the apparatus measured without scattering gas. In this experiment U_s, the voltage on the selector quadrupole was set at a given value and the voltage U_a on the analyzer quadrupole was scanned.

The various rotational states transmitted by the double "monochrometer" arrangement are identified in the figure. For the (2,0) and (3,0) states we note that the state analyzer voltage decreases with increasing voltage on the state selector. This behavior is expected: with increasing state selector voltage the image distance is reduced, to compensate for this the image distance of the state analyzer has to be increased for focussing on the detector at a fixed distance. The anomalous behavior of the (1,0) peak is due to the nonideal behavior caused by the large contribution of higher order Stark terms peculiar to this state. At high voltages there is some evidence in these experiments for nonadiabatic Δm transitions (see the next section) which can explain the small maximum at $U_s \simeq 8$ kV and state analyzer voltages above $U_a = 9$ kV.
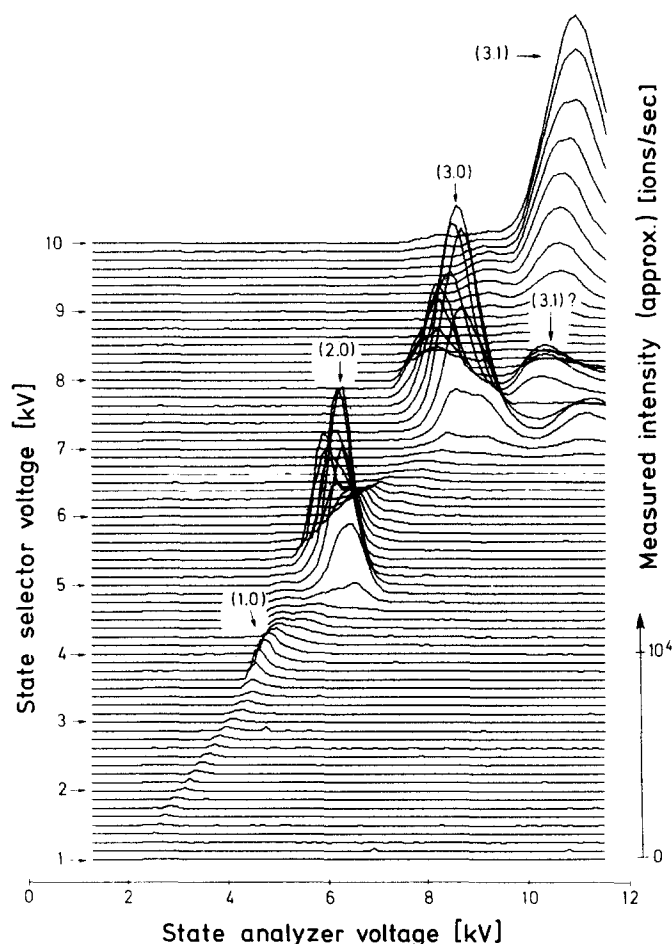
FIG. 3. The CsF beam signal measured at the detector is plotted as a function of the state analyzer voltage for various values of the state selector voltage. The CsF was seeded with Xe at an oven temperature of about 1000 K, $v_1 = 550$ m/s. Four main maxima are clearly resolved corresponding to double focussing of the $(j, m) = (1, 0)$, $(2, 0)$, $(3, 0)$, and $(3, 1)$ states. The small peak to the right of the $(3, 0)$ peak is attributed to a small amount of nonadiabatic transitions of the $(3, 0)$ molecules in the scattering region.

Of crucial importance for the state selection experiments is a high suppression of states other than the one focussed into the scattering region. This suppression was good for the $(2, 0)$ and $(3, 0)$ states. A typical measurement in which the state analyzer is used to scan for undesired rotational states in a beam transmitted by the state selector, which was set for the $(j, m) = (2, 0)$ state, is shown in Fig. 4.

The use of a Xe-seeded beam source is also expected to lead to a cooling of the vibrational degrees of freedom. Direct evidence for such cooling in a similar apparatus comes from the experiments of Bennewitz and Buess.[13] From their results we estimate the CsF vibrational temperature to be 150 ± 50 K. At this temperature the relative population of CsF in the $n = 0$, 1, and 2 states are 98%, 1.4%, and $\ll 1\%$, respectively. For a beam at equilibrium at 800 K the relative populations would be 56%, 28%, and 14%. Less direct evidence for vibrational cooling in our apparatus comes from highly resolved measurements of the voltage profile of the double fo-

cussed $(3, 0)$ state.[10b] Thus we estimate that 98% of the beam molecules were in the ground vibrational state and that 99% of the molecules were in the selected j state.

C. Polarization

The next question has to do with the purity of the selected m-state. This is specified by the degree of polarization P, which is defined as in Ref. 6b by

$$P = \frac{I(j, m) - \frac{1}{2j} \sum_{m' \neq m} I(j, m')}{\sum_{m'} I(j, m')}.$$ (2)

where $I(j, m)$ is the intensity at the detector with both quadrupoles set for the same state. For a pure beam in a single (j, m) state $P = 1$. For complete randomization $P = 0$. P can be measured directly by comparing the signal I_{opt} in a given (j, m) state under optimal conditions with the signal I_{rand} obtained with complete randomization. Complete randomization is easily achieved by grounding both the entrance aperture quadrants and the orientation field. From Eq. (2) it follows then that

$$P = (I_{opt}/I_{rand} - 1)/2j.$$ (3)

In all the runs P was always greater 0.75 and typically 0.90. Moreover P was greater for states with small j than for states with larger j.

Another more direct and sensitive measure of the polarization is possible by refocussing molecules in a state with different m value from that focussed into the scattering region. Such a test was possible with the $(3, 0)$ state since we were able to clearly resolve the $(3, 1)$ state. The focussing curve in Fig. 5 shows in an expanded scale the $(3, 1)$ signal obtained with the state selector set for the $(3, 0)$ state. The $(3, 1)$ intensity amounts to only about 90 ions/s or 9×10^{-3} of the $(3, 0)$ intensity. Assuming the same relative population in the
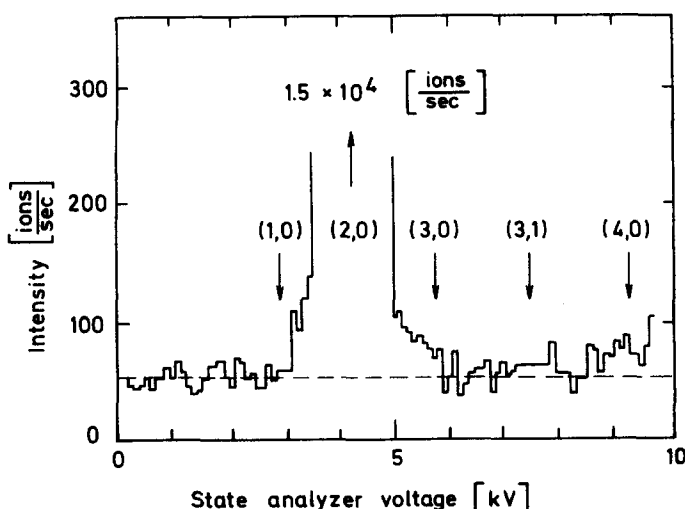

FIG. 4. The suppression of unwanted states is illustrated for the case of the $(2, 0)$ state. In the experiment the $(2, 0)$-state was focussed into the scattering region and the state analyzer voltage was swept to detect undesired states. In this experiment with the B configuration less than 30 ions/s were in the $(3, 0)$ state corresponding to a relative impurity of about 2×10^{-3}.
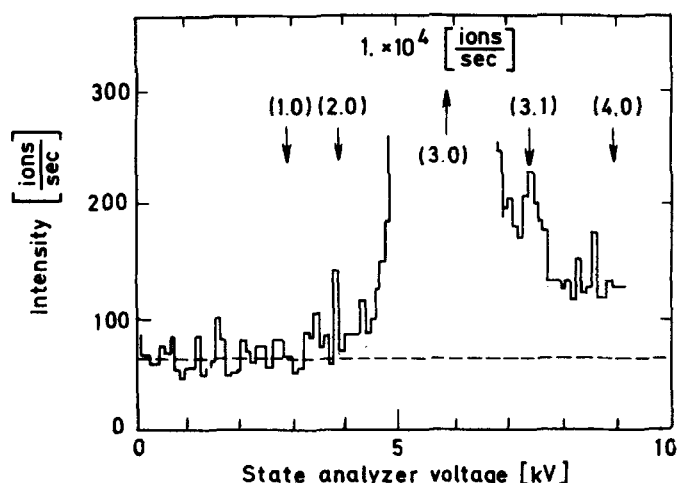
FIG. 5. The good degree of polarization of the state selected (3,0) beam is indicated by the small signal of undesired molecules in the (3,1) state found in a state analyzer focusing curve.

(3,2) and (3,3) states we get from Eq. (2) a polarization of 97% in this experiment.

No attempt was made to correct for the effect of depolarization on the measured cross sections. This was justified by noting that a simple calculation, for example, for $j = 2$ and $P = 0.75$ indicates that 80% of the molecules were in the desired (j, m) state. The other 20% contribute to the measured signal via other Δm transitions. The available results (Table IV) indicate however that the cross sections for $\Delta m = 0$ and $\Delta m = 1$ are the same within a factor 2 so that the resulting error is negligible compared to the relatively large statistical errors.

IV. MEASURING METHODS

Three different methods were used to determine the inelastic cross sections from the pressure dependence of the detector signals. For all the $\Delta m = 0$ transitions and for the $(3, 0) \rightarrow (3, 1)$ transition the method used previously was adopted.[6b] For the $(1, 1) \rightarrow (1, 0)$ and $(1, 1) \rightarrow (2, 0)$ transitions a different procedure was used.

A. Method used for the $\Delta m = 0$ transitions and the $(3,0) \rightarrow (3,1)$ transition

For the transition $i \rightarrow f$ the pressure dependence of the intensity in the states i and f in the scattering region is given by the following differential equations[6b]

$$dI(f) = I(i) \sigma_{app}^{i \cdot f} n\,dl - I(f) \sigma_{app}^{f} n\,dl \qquad (4)$$

$$dI(i) = I(f) \sigma_{app}^{f \cdot i} n\,dl - I(i) \sigma_{app}^{i} n\,dl \ , \qquad (5)$$

where $\sigma_{app}^{i \cdot f}$ is the effective integral *inelastic* cross section and σ_{app}^{i} is the effective integral *total* (sum over all final states) cross section for the state i. These cross sections are laboratory cross sections. The transformation into the center of mass system is discussed in a later section. The first term in Eq. (4) describes the production of "daughter" molecules in the final state f by inelastic collisions. The second term takes account of the attenuation of these newly formed daughter molecules by collisions in the scattering region. In Eq. (5)

the first term accounts for the gain of "mother" molecules due to inelastic collisions from the daughter state while the second term accounts for the attenuation of mother molecules.

To solve Eqs. (4) and (5) we assume $\sigma_{app}^{f \cdot i} \ll \sigma_{app}^{i}$ and $\sigma_{app}^{f \cdot i} \ll \sigma_{app}^{f}$ so that we can neglect the first term on the right side of Eq. (5). The remaining equations can be integrated to yield

$$I(f) = I_0(i)\,nl\,\sigma_{app}^{i \cdot f}\,\exp(-nl\,\sigma_{app}^{f})$$
$$\times \left\{ \frac{1 - \exp(-nl\,[\sigma_{app}^{i} - \sigma_{app}^{f}])}{nl\,[\sigma_{app}^{i} - \sigma_{app}^{f}]} \right\} + I_0(f)\exp(-nl\,\sigma_{app}^{f}) \ ,$$
$$(6)$$

where the index 0 refers to intensities in the scattering region measured without scattering gas. For the transitions studied the term in curly brackets lies between 0.95 and 1.05. This comes about, since $\sigma_{app}^{i} \simeq \sigma_{app}^{f}$. Since the statistical errors are larger than $\pm 5\%$, this term was set equal to 1.00 to yield:

$$I(f) = I_0(i)\,nl\,\sigma_{app}^{i \cdot f}\exp(-nl\,\sigma_{app}^{i}) + I_0(f)\exp(-nl\,\sigma_{app}^{f}) \ . \qquad (7)$$

The first term (I) on the right describes the gain in intensity due to inelastic scattering, while the second term (II) takes account of the attenuation of the background. The contributions I and II are shown in Fig. 6 for scattering from the (2.0) to the (1.0) and (3.0) states.

Equation (7) is used to determine $\sigma_{app}^{i \cdot f}$ from $I(f)$, $I_0(i)$ and $I_0(f)$. $I(f)$ is measured by setting the state selector for i and the analyzer for f and we designate this intensity therefore from here on by $I(i - f)$. Similarly $I_0(i)$ and $I_0(f)$ are determined from measurements (without scattering gas) with the state selector and analyzer set to correspond to $I_0(i - i)$ and $I_0(i - f)$, respectively. Later on in Sec. V we shall see how we take account of losses of molecules as they pass through the scattering
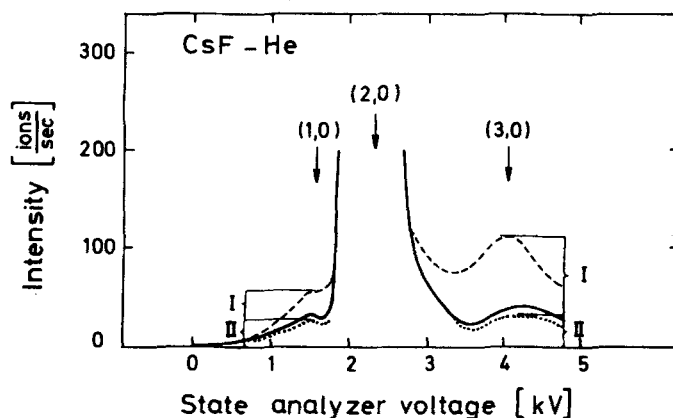

FIG. 6. The intensities $I(i-f)$ from which the effective laboratory inelastic cross sections are determined are indicated in an actually measured state analyzer focusing curve. The state selector is set for the (2, 0) state. The solid curve (—) shows the focussing curve measured without a scattering beam. The dashed curve (– – –) shows the intensity measured with a scattering beam. The dotted curve (· · ·) shows the estimated decrease in the residual intensity of the "daughter" state due to scattering. This decrease was determined from the measured total integral cross section for the final state f. The contributions I and II needed to determine the inelastic cross sections (2, 0) → (1, 0) and (2, 0) → (3, 0) are indicated in the diagram.
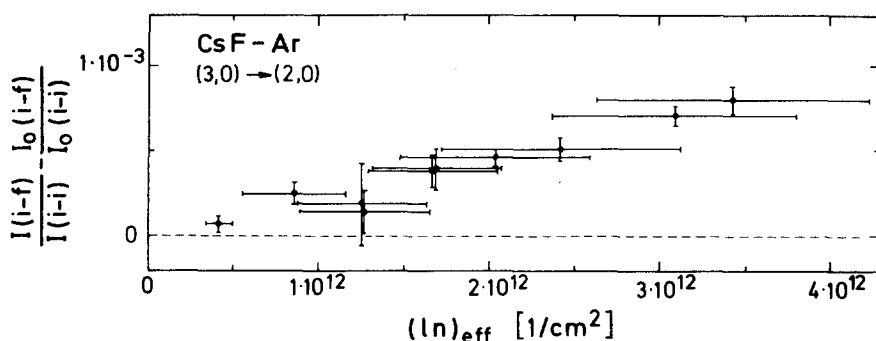
FIG. 7. The ratios of measured intensities are plotted as a function of the absolutely measured effective scattering path. The best fit slope of the straight line passing through the measured points yields the inelastic cross section. The example is for the $(3, 0) \rightarrow (2, 0)$ transition in the scattering from Ar in the configuration B. The errors in the ordinate are statistical errors, whereas the errors in the abscissa are the maximum errors in the absolute determinations.

region in the interpretation of $\sigma_{app}^{i \rightarrow f}$. To further simplify Eq. (7) we take advantage of the similarity between σ_{app}^{i} and σ_{app}^{f} noted above and set them equal. This means that $I(i-i)/I_0(i-i) = I(f-f)/I_0(f-f)$. Furthermore by introducing the experimentally measured quantity $(n \times l)_{eff}$ (see Sec. IV D) for $n \times l$ we can rewrite Eq. (7) as

$$\sigma_{app}^{i \rightarrow f} = \frac{1}{(nl)_{eff}} \left[\frac{I(i-f)}{I(i-i)} - \frac{I_0(i-f)}{I_0(i-i)} \right] . \qquad (8)$$

In an actual measurement the state selector was switched between two states [say (2, 0) and (3, 0)] and the state analyzer probed three states (say (1, 0), (2, 0), and (3, 0)). The intensities were measured for 5 to 10 different target source pressures and in this way the cross sections for four transitions [(2, 0)→ (1, 0), (2, 0)→ (3, 0), (3, 0)→ (1, 0), and (3, 0)→ (2, 0)] are measured simultaneously. Figure 6 shows in the appropriate focussing curve some of the intensities measured for one target gas pressure in scattering from He. Because of the low intensities and small differences a typical measurement of one cross section took about three hours.

Figure 7 shows some representative measurements of the difference of intensity ratios [see Eq. (8)] as a function of $(n \times l)_{eff}$ for CsF–Ar. In all the measurements the Nalimov test[15] was used to discard values with a probability of less then 0.1%. The absolute inelastic cross sections were determined from the slope of such curves using the maximum likelihood method.[16] The errors in the intensity ratio difference (statistical errors) as well as in $(n \times l)_{eff}$ (maximum error, see Sec. I) were included to yield the standard deviations shown in Table II.

B. Method used for the (1,1) → (1,0) transition

Molecules in the (1, 1) state cannot be focussed with electrostatic quadrupole fields since their Stark effect energy decreases with field strength. However, molecules in this state can be produced in the scattering region by intentionally depolarizing a (1, 0) beam by grounding the four electrodes of the entrance aperture in front of the scattering region. From the polarization studies on the (3, 0) and (3, 1) states reported in Sec. III C we know that this leads to a complete randomiza-

tion of states. Then by setting the state analyzer for the (1, 0) state it is possible to obtain information on the (1, 1)→ (1, 0) cross sections by comparing the intensities obtained with and without depolarization. The same applies to the (1, 1)→ (2, 0) transition. Since the procedure for extracting cross sections from the measured intensities is, however, somewhat different for the (1, 1) → (1, 0) and (1, 1)→ (2, 0) transitions we discuss first the (1, 1)→ (1, 0) transition.

To describe the relative population of molecules in the (1, 1) state we introduce the parameter a defined by

$$a = I_0(1, 1)/I_0(1, 0) . \qquad (9)$$

For a completely depolarized beam $a_{dep} = 2$ since the (1, +1) and (1, -1) states have an intensity equal to that of the (1, 0) state. For the polarized beam a_{pol} will depend on the polarization of the beam; for $P = 1$, $a_{pol} = 0$. It can be shown in a manner analogous to Eq. (9) that a_{pol} is given by

$$a_{pol} = [3 I_{0_{dep}}(1, 0-1, 0)/I_{0_{pol}}(1, 0-1, 0)] - 1 . \qquad (10)$$

Thus the signal measured with the state analyzer set for the (1, 0) state can be obtained by applying Eq. (7). It will depend on whether the aperture electrodes have the optimal voltage (subscript pol):

$$I_{pol}(f-f) = a_{pol} I_{0_{pol}}(f-f) (nl)_{eff} \sigma_{app}^{i \rightarrow f} \exp(- (nl)_{eff} \sigma_{app}^{i})$$
$$+ I_{0_{pol}}(f-f) \exp(- (nl)_{eff} \sigma_{app}^{f}) \qquad (11)$$

or are grounded (index dep):

$$I_{dep}(f-f) = 2 I_{0_{dep}}(f-f) (nl)_{eff} \sigma_{app}^{i \rightarrow f} \exp(- (nl)_{eff} \sigma_{app}^{i})$$
$$+ I_{0_{dep}}(f-f) \exp(- (nl)_{eff} \sigma_{app}^{f}) , \qquad (12)$$

where $i = (1, 1)$ and $f = (1, 0)$. Equations (11) and (12) can be solved to yield

$$(nl)_{eff} \sigma_{app}^{i \rightarrow f} = \left\{ \frac{I_{dep}}{I_{0_{dep}}} - \frac{I_{pol}}{I_{0_{pol}}} \right\} \frac{\exp(- (nl)_{eff} \sigma_{app}^{i})}{2 - a_{pol}} , \qquad (13)$$

where the notation has been further simplified since both selectors are set for the state f. $\sigma_{app}^{(1, 1)}$ cannot be measured directly and was therefore assumed to be given by $\sigma_{app}^{(1, 0)}$ which was determined from $I_{pol}/I_{0_{pol}}$. Thus $\sigma_{app}^{(1, 1) \rightarrow (1, 0)}$ depends directly on the small difference between the two ratios $I_{dep}/I_{0_{dep}}$ and $I_{pol}/I_{0_{pol}}$ and as a result, large statistical errors are expected.

C. Method used for the (1,1) → (2,0) transition

For this transition the formula corresponding to Eq. (11) is:

$$I_{pol}(h-f) = I_{0_{pol}}(h-h)(nl)_{eff}\, \sigma_{app}^{h-f}\exp(-(nl)_{eff}\,\sigma_{app}^{h})$$
$$+ a_1 I_{0_{pol}}(h-h)(nl)_{eff}\,\sigma_{app}^{i-f}\exp(-(nl)_{eff}\,\sigma_{app}^{i})$$
$$+ I_{0_{pol}}(f-f)\exp(-(nl)_{eff}\,\sigma_{app}^{f})\ , \qquad (14)$$

where $h = (1,0)$, $i = (1,1)$, and $f = (2,0)$. Again we assume $\sigma_{app}^{(1,0)} = \sigma_{app}^{(1,1)} = \sigma_{app}^{(2,0)}$ and determine these from $I_{pol}/I_{0_{pol}}$ measured for the $(1,0) \rightarrow (1,0)$ arrangement with the result

$$R_{pol} = \frac{I_{pol}(h-f)}{I_{pol}(h-h)} - \frac{I_{0_{pol}}(h-f)}{I_{0_{pol}}(h-h)} = (nl)_{eff}\,[\sigma_{app}^{h-f} + a_{pol}\,\sigma_{app}^{i-f}]\ .$$
$$(15)$$

A similar result holds for the depolarized beam. The final result for the inelastic cross section is

$$(nl)_{eff}\,\sigma_{app}^{i-f} = \frac{R_{dep} - R_{pol}}{2 - a_{pol}}\ . \qquad (16)$$

Since R_{dep} is roughly a factor of 2 larger than R_{pol}, the scatter in $\sigma_{app}^{(1,1)-(2,0)}$ is smaller than for the $(1,1) \rightarrow (1,0)$ transition.

D. The determination of absolute cross sections

The absolute effective scattering path in the target beam is given by

$$(nl)_{eff} = \int_{-\infty}^{+\infty} n(l)\,dl\ , \qquad (17)$$

where n is the particle density and l is the distance in the primary beam direction measured from the axis of the secondary beam. To determine $(nl)_{eff}$ we note that the total flow Q (particles/s) in the secondary beam is given by

$$Q = 2\pi \int_0^\infty n(z,r)\,r\,dr \int_0^\infty v f(v)\,dv\ , \qquad (18)$$

where z is the distance from the nozzle, r is the radius in a plane perpendicular to z and $f(v)$ is the velocity distribution of the secondary nozzle beam. The last integral can be replaced by $\hat{u}$, the most probable velocity of the secondary beam. Since the atoms move along straight lines emanating from the nozzle the density decreases with z^{-2} and $\int n(z,r)\,dr$ decreases with z^{-1}. Thus with Eq. (18) we can rewrite Eq. (17) as

$$(nl)_{eff} = \frac{Q}{\pi \hat{u}} \frac{z'}{z} \frac{\displaystyle\int_0^\infty \tilde{n}(z',r)\,dr}{\displaystyle\int_0^\infty \tilde{n}(z',r)\,r\,dr}\ , \qquad (19)$$

where z' is the distance at which the normalized dimensionless density distribution $\tilde{n}(z',r)$ $(= n(z',r)/n(z',0))$ is determined, while z is the distance at which the primary beam crosses the secondary beam. To determine $(nl)_{eff}$ absolutely, we need to measure Q, $\hat{u}$ and the dimensionless density distribution $\tilde{n}(z',r)$.

Q was measured in the following way: For a given nozzle and source pressure P_0 the pressure rise in the scattering chamber (chamber IV in Fig. 2) was mea-

sured with an ionization gauge. Then in a separate experiment an absolutely measured gas flux was admitted into the scattering chamber at a region near the skimmer. The gas flux which had to be admitted to produce the same pressure increase on the same gauge was then obtained. A dynamic expansion method very similar to the device used by Bennewitz et al.[1] was used to determine the absolute flux. This method has the advantage of being independent of the type of gas used and has an absolute accuracy of better than 2%. In the range studied Q was found to be a linear function of P_0. For Kr at $P_0 = 10^3$ Torr, Q is 10^{-3} Torr liter/sec. The most probable velocity of the rare gas beams was calculated assuming a complete isentropic expansion. Experiments show this to be an excellent approximation provided condensation does not occur.[18] For the molecular gases u varies slightly with P_0. This was taken into account in the evaluation of Eq. (18). For N_2, CO, CO_2, CF_4, SF_6, CHF_3, and C_2H_6, u was measured as a function of P_0 directly in another apparatus equipped with a time of flight velocity analyzer.[19] The other values were estimated from these measured values. Finally normalized distributions $\tilde{n}(z',r)$ were measured for each gas with a pitot-tube detector (an enclosed ionization gauge with a long entrance channel for the beam) which could be displaced along the primary beam directions. Similar pitot tube detectors have been found to be linear over a wide range of pressures.

This method of determining absolute cross sections was checked by comparison with cross sections determined in the following alternative independent manner. Absolute integral total cross sections were first determined for scattering of the nonstate selected beam from diffuse gas admitted into the scattering chamber. Since the length is known, it was only necessary to determine the absolute pressure. For this purpose the ionization gauge in the scattering chamber was absolutely calibrated using the dynamic expansion method used previously. The absolute values were then converted into effective cross sections for scattering from a nozzle target beam using standard procedures.[42] From the attenuation measured with a nozzle target beam it is easily possible using Beer's law to determine the absolute effective scattering path $(nl)_{eff}$. $(nl)_{eff}$ values determined in this way, were in reasonable agreement with the previously determined values for Ar, Kr, and Xe.[20]

V. RESULTS

Table II summarizes all the available results for the inelastic scattering of CsF. In the experiments with the rare gases two different geometric configurations denoted by A and B (see Sec. II) were used. As a result of the different acceptance angles the measured cross sections were also found to be different. Due to the inclusion of additional more recent measurements some of these results deviate somewhat from those published previously.[8]

A number of general trends are worth noting here. A more detailed discussion of the results in terms of the interaction potential will be postponed until a later section. First we note that microscopic reversibility ap-

TABLE II. Measured values of $\sigma_{app}^{i \to f}$ in Å^2 for 9 transitions of CsF scattering from 18 different target gases. The errors are estimated standard deviations (see Sec. IV D). The CsF primary beam velocity was 480 m/s for the apparatus configuration A and 550 m/s for the configuration B.

Gas	Configuration	$\Delta j=1$, $\Delta m=0$				$\Delta j=2$ $\Delta m=0$	$\Delta j=1$, $\Delta m=1$		$\Delta j=0$, $\Delta m=1$	
		$(1,0) \to (2,0)$	$(2,0) \to (1,0)$	$(2,0) \to (3,0)$	$(3,0) \to (2,0)$	$(3,0) \to (1,0)$	$(1,1) \to (2,0)$	$(2,0) \to (3,1)$	$(1,1) \to (1,0)$	$(3,0) \to (3,1)$
He	A	...	3.9±0.5	7.2±2.5	3±1	0.9±0.3	...	...	...	...
	B	17±4	3±1	...	...	...	2.9±2	7±2	...	...
Ne	A	...	4±1.5	5.6±1	1.6±0.5	0.8±0.3	...	...	...	...
	B	13±3	3.5±1	3±1	2.2±0.5	...	3.1±1	2.5±1	4.1±3	5.5±2
Ar	A	...	4.4±1.5	5.7±1	2.4±1	0.6±0.3	...	...	...	...
	B	14±3	...	3.2±1	2.2±1	...	5.1±2	2.3±1	5±4	4.5±2
Kr	A	...	1.9±1	4±1	2.3±0.5	0.5±0.3	...	...	...	...
	B	13±3	...	2.5±1	1.9±0.5	...	5.4±2	2±1	7±4	4.5±2
Xe	A	...	3±1	5±1	3.5±1	0.7±0.3	...	...	...	...
CH_4	A	...	2.7	6.3	4.0	0.8	...	...	...	...
CF_4	A	...	2.3	6.5	4.7	1.2	...	...	...	...
SF_6	A	...	2.2	4.7	2.4	0.5	...	...	...	...
C_2H_6	A	...	4.3±1.2	13.8±3.3	7.8±2.1	0.25±0.1	...	...	...	...
N_2	A	...	10±3.5	47±12	29±8	0.65±0.2	...	...	...	...
CO	A	...	12.2±3.6	54±12	43±10	0.8±0.2	...	...	...	...
CO_2	A	...	19.2±5.6	96±25	74±28	1.8±0.5	...	...	...	...
N_2O	A	...	14	94	91	2.3	...	...	...	...
CH_3Cl	A	...	28	165	194	8.2	...	...	...	...
CH_3Br	A	...	23	151	127	5.6	...	...	...	...
CF_3H	A	...	135±50	620±170	420±115	17±5	...	...	...	...
CF_3Cl	A	...	29	207	196	6.5	...	...	...	...
CF_3Br	A	...	33	225	217	7.5	...	...	...	...

pears to be violated: The $(1,0) \to (2,0)$ cross sections are much larger than the $(2,0) \to (1,0)$ cross sections. This apparent contradiction is resolved when complete account is taken of the different effective apertures resulting from the different trajectories of the $(2,0)$ and $(1,0)$ molecules in the quadrupole fields as discussed in the next section. The same holds for the $(2,0) \to (3,0)$ and $(3,0) \to (2,0)$ transitions. With but one exception, the measured effective cross section for the $(2,0) \to (3,0)$ transition is largest confirming this interpretation. Next we observe that the $(3,0) \to (1,0)$ cross section is smaller by an order of magnitude or more. This large difference is due to the smaller coupling for the $\Delta j=2$ transitions. The cross sections for the $(1,1) \to (2,0)$ transitions for the rare gases are considerably smaller than those for the $(1,0) \to (2,0)$ transition. The difference is not nearly so large for the $(2,0) \to (3,1)$ cross section compared to the $(2,0) \to (3,0)$ cross sections. Finally we find that the pure Δm cross sections are of about the same size as the Δj cross sections. In order to discuss these results in terms of the anisotropic po-

tential, it is necessary to take account of the state dependent transmission of the apparatus and transform the results into the center of mass system. Transformed center of mass differential cross sections for the $(2,0) \to (3,0)$ transition are listed in Table III [see also Eq. (43b)] for all target gases.

VI. RELATIONSHIP OF THE MEASURED CROSS SECTIONS TO THE CENTER OF MASS CROSS SECTIONS

In order to compare the measured cross sections with the theoretical predictions it is necessary to take account of the finite range of scattering angles which is accepted by the apparatus. Because of the rather complicated geometry of the apparatus this was only possible by carrying out a Monte Carlo simulation of trajectories passing through the apparatus. From the trajectory study a transmission function is obtained, which also takes account of the transformation from the center of mass to the laboratory system.

TABLE III. The inelastic differential cross section parameters σ_0^{i-f} for the $(2,0) \rightarrow (3,0)$ transition (A configuration) are listed for all the scattering target gases.

Target gas	A_n	n	s	η	$\sigma_0 \mathscr{S}_0^{-\eta}$ [Å²/sr]	σ_0
He	$\alpha\mu Q$	7	6	$\frac{1}{3}$	$(0.249\times10^2)^a$	$(5.35)^a$
Ne	$\alpha\mu Q$	7	6	$\frac{1}{3}$	0.270×10^3	58.1
Ar	$\alpha\mu Q$	7	6	$\frac{1}{3}$	0.736×10^3	159
Kr	$\alpha\mu Q$	7	6	$\frac{1}{3}$	1.298×10^3	279
Xe	$\alpha\mu Q$	7	6	$\frac{1}{3}$	2.549×10^3	549
CH_4	$\alpha\mu Q$	7	6	$\frac{1}{3}$	0.212×10^3	45.0
CF_4	$\alpha\mu Q$	7	6	$\frac{1}{3}$	2.195×10^3	473
SF_6	$\alpha\mu Q$	7	6	$\frac{1}{3}$	2.612×10^3	563
C_2H_6	μQ	4	4	1	0.225×10^4	22.5
N_2	μQ	4	4	1	0.731×10^4	73.1
CO	μQ	4	4	1	0.820×10^4	82.0
CO_2	μQ	4	4	1	2.324×10^4	232
N_2O	μQ	4	4	1	2.197×10^4	220
CH_3Cl	$\mu\mu$	3	3	$\frac{4}{3}$	0.427×10^5	92.1
			(6)	$(\frac{5}{3})$		(13.1)
CH_3Br	$\mu\mu$	3	3	$\frac{4}{3}$	0.574×10^5	123
			(6)	$(\frac{5}{3})$		(15.7)
CF_3H	$\mu\mu$	3	3	$\frac{4}{3}$	1.918×10^5	426
			(6)	$(\frac{5}{3})$		(56.7)
CF_3Cl	$\mu\mu$	3	3	$\frac{4}{3}$	0.807×10^5	175
			(6)	$(\frac{5}{3})$		(21.6)
CF_3Br	$\mu\mu$	3	3	$\frac{4}{3}$	1.046×10^5	226
			(6)	$(\frac{5}{3})$		(26.4)

^{a}The results for He are much less reliable than for the heavier targets. This is because the range of center of mass scattering angles probed for He is large and the simple power law angular dependence is probably not as good as for the other targets.

A. Simulation procedure

To simulate the trajectories in the apparatus a number of assumptions are required. First it is assumed that the apparatus was ideally adjusted and corresponded to the construction plans. Indeed as mentioned in Sec. II a very high accuracy in the alignment (± 0.03 mm) was achieved. Test calculations showed that deviations in the transverse positions of apertures and obstacles of ± 0.03 mm had no appreciable influence on the results extracted from the computed trajectories.

More crucial is the simulation of trajectories in the quadrupole field. Here it is necessary to assume both an approximate form of the field distribution and to approximate the electric field dependence of the Stark effect. Although cylindrical rods were used, it was assumed that the equipotential lines were those of a perfect hyperbola:

$$V(x,y) = V_0 \frac{x^2 - y^2}{R_0^2} , \qquad (20)$$

where x and y are measured from the central axis of the

quadrupole and R_0 is the distance from the axis to the surface of one of the rods. Dayton et al.[21] have shown that the error in $V(x,y)$ is reduced by choosing $r_0/R_0 = 1.16$ (where r_0 is the rod radius). Everdij et al.[22] have obtained an expansion for the field in an arrangement similar to ours. The error in assuming Eq. (20) is smaller than $0.02\,(r/R_0)^6$, where $r^2 = x^2 + y^2$, and since r/R_0 was always less than 0.8, the error in the field distribution is negligibly small.

The Stark effect energy is obtained from perturbation theory as an expansion in powers of λ ($=\mu_0 E/B$, where μ_0 is the dipole moment, E the electric field, and B the rotational energy constant):

$$\epsilon(\lambda) = \epsilon_0 + \epsilon_2 \lambda^2 + \epsilon_4 \lambda^4 + \epsilon_6 \lambda^6 + \cdots , \qquad (21)$$

where $\epsilon_0 = j(j+1) B$ and ϵ_2 is given by

$$\epsilon_2 = (j(j+1) - 3m^2)/2j(j+1)(2j-1)(2j+3) . \qquad (22)$$

An expression for ϵ_4 can be found in Wharton et al.[23] A closed expression for ϵ_6 is only known for the $(1,0)$ state. $\epsilon(\lambda)$ can also be calculated exactly by solving a continuous fraction.[24] The results have been tabulated for a large number of rotational states.[25] For all but the $(1,0)$ state $\epsilon(\lambda)$ was approximated using Eq. (21) with terms up to ϵ_6. ϵ_6 was obtained from the difference between the exact results and those calculated using the perturbation expressions for ϵ_2 and ϵ_4. This procedure proved unsatisfactory for the $(1,0)$ state since the convergence radius is $\lambda \leq 2^{26}$ and for this state the exact results were fitted to a cubic spline expression. With these approximations it was possible to simulate the trajectories in a single quadrupole field. In a typical application the trajectories were started on a plane located at the skimmer opening with randomly chosen coordinates and with a randomly chosen angle within the range of angles accepted by the apparatus. Each trajectory was followed through until it struck an obstacle, an aperture or arrived at the desired destination, i.e., either the scattering region or the detector. The triangular velocity distribution of the primary velocity distribution was also averaged over by a Monte Carlo procedure. This distribution was assumed to be independent of entrance angle.

B. The apparatus transmission function

To define the apparatus transmission function we recall the discussion of Sec. IV and consider first for simplicity only a very thin target beam. This corresponds to considering only the first term on the right in Eq. (4) and the corresponding expression for σ_{app}^{i-f} is

$$\sigma_{app}^{i-f} = \frac{1}{(nl)_{eff}} \frac{I(i-f)}{I(i-i)} . \qquad (23)$$

The signal $I(i-f)$ can be derived directly from the phenomenological equation for the scattering intensity in a differential scattering experiment, which can be written as[2]

$$I(i-f) = \iiint d^3 v_a \iiint d^3 v_b \iiint d^3 l \iint d^2 \Omega \, \Delta N^{i-f} , \qquad (24)$$

where

$$\Delta N^{i-f} = n_a^i \, f^3(v_a) \, n_b \, f^3(v_b) g \, \frac{d^2 \sigma}{d^2 \omega} \, (\vartheta, \varphi, g) \left| \frac{d^2 \omega}{d^2 \Omega} \right| \qquad (25)$$

$n_a^i \, f^3(v_a)$ and $n_b \, f^3(v_b)$ are the phase space densities of the primary beam in state i and the target beam, respectively, $f^3(v)$ are the velocity distributions, $d^2\sigma/d^2\omega$ is the center of mass differential cross section and $d^2\omega/d^2\Omega$ is the Jacobian for the transformation of solid angles from the laboratory into the center of mass system. The integrals in Eq. (24) take account of all the smearing from the apparatus velocity distributions and geometry. It is more convenient to rewrite Eqs. (24) and (25) as

$$I(i - f) = \dot{N}_a^{(i)} \iiint d^3 v_a \iiint d^3 v_b \iint d^2 \Omega \int n_b \, dl \qquad (26)$$

$$f^3(v_a) \, f^3(v_b) \hat{g}/v_a \, \frac{d^2 \sigma}{d^2 \omega} \, (\vartheta, \varphi, \hat{g}) \left| \frac{d^2 \omega}{d^2 \Omega} \right|$$

with

$$\dot{N}_a^{(i)} = \iiint n_a^i \, v_a \, d^2 l \qquad (27)$$

the beam intensity of molecules a in state i entering the scattering region. By assuming that $d^2\sigma/d^2\omega$ is only weakly dependent on the relative velocity we have replaced g by $\hat{g}$, which is the most probable relative velocity ($\hat{g}^2 = \hat{v}_a^2 + \hat{v}_b^2$, where $\hat{v}_a$ and $\hat{v}_b$ are the most probable velocities). We define the transmission function T^{i-f} by replacing the many integrals on the right hand side of Eq. (26) by a single integral:

$$I(i - f) = \dot{N}_a^{(i)} (nl)_{\text{eff}} \int_0^\tau \int_0^{2\pi} T^{i-f}(\vartheta, \varphi) \frac{d^2 \sigma}{d^2 \omega} (\vartheta) \sin\vartheta \, d\vartheta \, d\varphi \, , \qquad (28)$$

where we have set $\int n_b(l) \, dl = (n_b l)_{\text{eff}}$. Before describing how we obtain T^{i-f} we recall from Eq. (8) that the other quantity used in the measurement of $\sigma_{\text{app}}^{i-f}$ is $I_0(i - i)$. This is given in similar fashion by

$$I_0(i - i) = \dot{N}_a^{(i)} \iiint d^3 v_a \, f^3(v_a) \, , \qquad (29)$$

where the integral not only takes account of the velocity smearing but also implicitly takes account of the loss of molecules of type a in passing from the scattering region to the detector. Analogously to Eq. (28) we define another transmission function for the intensity observed without scattering by

$$I_0(i - i) = \dot{N}_a^{(i)} \, T^{i-i}(\vartheta = 0, \, \varphi = 0) \, . \qquad (30)$$

Thus from Eq. (23) we obtain the following expression for $\sigma_{\text{app}}^{i-f}$

$$\sigma_{\text{app}}^{i-f} = 2\pi \, \frac{\hat{g}}{v_a} \int_0^\tau \eta(\vartheta) \frac{d^2 \sigma}{d^2 \omega} (\vartheta) \sin\vartheta \, d\vartheta \, , \qquad (31)$$

where

$$\eta(\vartheta) = \frac{1}{2\pi} \int_0^{2\pi} \frac{T^{i-f}(\vartheta, \varphi)}{T^{i-i}(0, 0)} \, d\varphi \, , \qquad (32)$$

is called the reduced transmission function.

Both T^{i-f} and T^{i-i} were calculated using the simulation program. First of all the quantity $T^{i-f}(\vartheta, \varphi)$ was determined by calculating the probability that a particle, which had changed its state from i to f after scattering through the center of mass angles ϑ and φ, would arrive
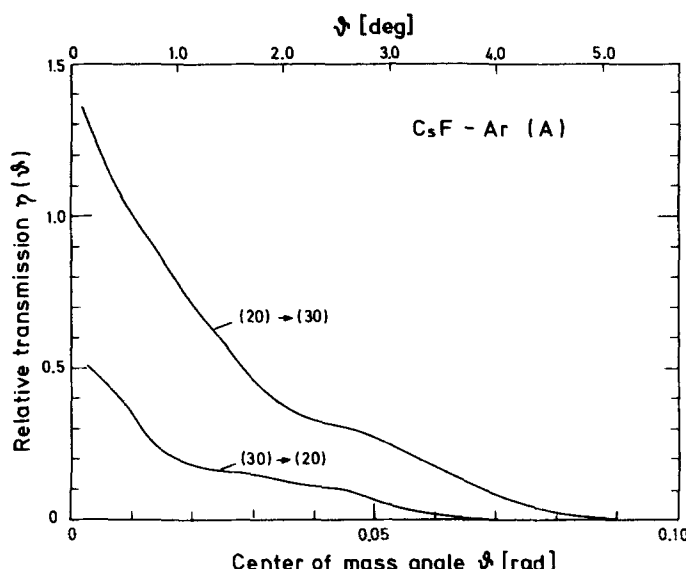

FIG. 8. The calculated transmission function is plotted as a function of the center of mass scattering angle ϑ for the $(2,0) \rightarrow (3,0)$ transition and for the $(3,0) \rightarrow (2,0)$ transition for CsF scattered from Ar in the A apparatus configuration. Note that the probability of an inelastically scattered particle being transmitted to the detector, is more than a factor 3 larger for the $(2,0) \rightarrow (3,0)$ than for the $(3,0) \rightarrow (2,0)$ transition.

at the detector. $T^{i-f}(\vartheta, \varphi)$ is always less than one since depending on the vector velocities of the collision partners the scattered molecule can strike against one of the apertures or obstacles before arriving at the detector. $T^{i-i}(\vartheta = 0)$ is determined in a similar fashion. It is simply obtained from the ratio of the number of particles in state i, which arrive at the detector (no scattering!) divided by the total number of particles, which arrive in the scattering region. $T^{i-i}(\vartheta = 0)$ is also always less than one. However, as we shall see below, $\eta(\vartheta)$ may be greater than one since the chances of striking the detector may be improved, if a particle has changed its state from i to f as a result of a more favorable Stark effect $\epsilon(\lambda)$ in the new state f. In the simulation the distributions discussed in the preceding subsection A were used. For simplicity the target beam velocity distribution was also assumed to be triangular with a relative halfwidth of 10% FWHM for all gases. The angular distributions of the target beam and the finite extent of the scattering region were included. $T^{i-f}(\vartheta)$ was calculated for 20 angles in the range of angles of interest. For each angle several 10^4 trajectories were calculated. For one scattering gas the total computing time amounted to 15 min for all but the $(1,0)$ state and up to 2 h for the $(1,0)$ state.

Figure 8 shows typical transmission functions for the $(2,0) - (3,0)$ and the $(3,0) - (2,0)$ transitions. The curves show as expected that the probability of transmission is greater for particles scattered through the smallest angles. The structure in the curves comes from the unusual double-cone solid angular region within which molecular trajectories enter and leave the scattering region. Perhaps most surprising is the fact that the reduced transmission function for $(2,0) - (3,0)$ is greater than 1 for $\vartheta = 0$ but definitely smaller than 1 for the

$(3, 0) \rightarrow (2, 0)$. This reflects the fact that $(3, 0)$ molecules have more ideal trajectories in the quadrupole fields than the $(2, 0)$ molecules. Thus in the transition $(2, 0) \rightarrow (3, 0)$ the $(3, 0)$ molecules have a better chance of reaching the detector for small angles than if they had remained in the $(2, 0)$ state. These differences in the transmission function explain the apparent breakdown of microscopic reversibility in the measured cross sections.

The transmission functions for all the rare gases and for most of the transitions of Table II are available in tabular form.[27]

For the other gases an approximate procedure has been resorted too. In view of the uncertainties in the potential and scattering theory for the other systems this procedure is justifiable. First we note that in first approximation the $\eta(\vartheta)$ functions must be related to a universal transmission function depending only on the laboratory angle Θ. To check this we have used a small angle transformation equation

$$\Theta = \frac{\mu}{m_a} \sqrt{\frac{g}{v_a}} \, \vartheta_{cm} \tag{33}$$

to convert all the rare gas $\eta(\vartheta)$ functions for the $(2, 0) \rightarrow (3, 0)$ transition into the laboratory system and find that the data are nearly consistent with one curve. The following formula was found to work well for scattering angles from 0 up to 10 mrad.

$$\eta^{20 \rightarrow 30}(\Theta) = 2 - \left(\frac{\Theta}{\Theta_0}\right)^{0.5} \tag{34a}$$

where $\Theta_0 = 3.5$ mrad. At larger angles ($\Theta > 13$ mrad) the best fit was given by

$$\eta^{20 \rightarrow 30}(\Theta) = 2 - \left(\frac{\Theta}{\Theta_0}\right)^{0.4} \tag{34b}$$

In the intermediate region between 10 and 13 mrad, a linear combination was used:

$$\eta^{20 \rightarrow 30}(\Theta) = f(\Theta)\left[2 - \left(\frac{\Theta}{\Theta_0}\right)^{0.5}\right] + g(\Theta)\left[2 - \left(\frac{\Theta}{\Theta_0}\right)^{0.4}\right] \tag{35}$$

with $f(\Theta) = (13 - \Theta)/3$ (Θ in mrad) and $g(\Theta) = \Theta - 10/3$. These equations are only valid for small angles for which $\eta \geq 0$. A simpler—but less accurate—approximation is to use Eq. (34a) over the entire angular region.

Thus in comparisons of theory with experiment the procedure is to calculate the differential cross section and use Eq. (31) to convolute with the reduced transmission function. For the rare gases the exact results[27] can be used. For the other systems one can use the expressions Eq. (34) and (35). With the aid of Eq. (33) the angles are converted into the center of mass system for the partners in question and the resulting $\eta(\vartheta)$ used in Eq. (31).

VII. DISCUSSION IN TERMS OF ANISOTROPIC POTENTIALS

The measured inelastic cross sections are very sensitive to the anisotropy of the potential. Since only small angle scattering contributes to the cross sections, most of the scattering takes place in the long range attractive part of the potential. The long range aniso-

tropic potential in the case of CsF interacting with atoms and molecules is largely dominated by either classical induction terms or electrostatic terms which are easily calculated.[28] The contribution from quantum mechanical dispersion forces can be estimated using perturbation theory.[28] The observation of only the small angle part of the inelastic scattering has the additional advantage that because of the relatively weak interaction in many cases first-order-scattering theory (e.g. Born approximation) can be used to interpret the results. For more accurate comparisons the sudden approximation[29] or high energy approximation[29] as well as the infinite order sudden approximation[30] are needed. In semiclassical approximations the translational motion can be well represented by a straight-line trajectory since the center of mass scattering angle is less than about 2° (see Fig. 8). A constant velocity can be assumed as well since the energy transfer $\Delta E/E$ is only of the order 10^{-3}.

For the structureless rare gas atom targets the interpretation is most straightforward since we do not have to account for rotational (and vibrational) transitions of the target. For this reason a detailed accurate comparison of the results with theory is only possible at the present time for the rare gases. Such work has recently been carried out by Dickinson and Richards[31] and will also be the subject of a subsequent paper.[32] In this section we shall attempt to interpret some of the cross sections for all the gases in a less exact manner by the aid of the Born approximation and the approximate expressions Eqs. (34) and (35) for the transmission function. The advantage of this simple approach is that it enables us to "invert" the data and obtain molecular constants and properties from the cross sections. Our major aim here however will be (i) to test this procedure, and (ii) to use it to try to obtain a more quantitative and convincing identification than hitherto possible of the predominant terms in the long range potential leading to the observed inelastic cross sections in the different target gases.

A major assumption in this analysis is that the observed transitions are due largely to direct collisions. Van de Ree[33] has pointed out that orbiting may occur in collisions of TlF with Ar up to fairly high relative energies corresponding to $E_{cm}/\epsilon \lesssim 5$ (ϵ is the potential well depth). Orbiting is well established in atom–atom collisions[34] where it occurs for $E_{cm}/\epsilon \lesssim 0.8$. Since we do not know the potential well depth ϵ for these systems with any great accuracy,[35] it is difficult to assess the energies at which orbiting is possible. Orbiting and complex formation would appear to be most probable in the collisions of CsF with the symmetric top molecules where the strong dipole–dipole forces are effective. Rather convincing evidence against the importance of orbiting collisions however comes from the relative measured probabilities for the transitions with different Δj. If the formation of long lived complexes with extensive equilibration of the internal degrees of freedom were to occur, then we expect the populations of the various final states to be in near thermodynamic equilibrium or in the order $(1, 0) > (2, 0) > (3, 0)$ for any given initial state. If equilibration were to occur, then the probability for a transition $(3, 0) \rightarrow (1, 0)$ would be greater

than say for a transition $(3,0) \to (2,0)$ after due allowance for the different transmission functions. The data in Table II show that this definitely does not hold for any of the systems. Thus we regard this result as evidence that complex formation is not an important process for any of these collisions.

For a quantitative analysis of the data the following major assumptions are made:

(1) The inelastic differential cross section is given by

$$\frac{d^2\sigma^{i\to f}}{d^2\omega}\, (E_{\text{cm}}, \vartheta) = P^{i\to f}(b(\vartheta))\, \frac{d^2\sigma}{d^2\omega}\,(E_{\text{cm}}, \vartheta)\Big|_{el}\,, \tag{36}$$

where $P^{i\to f}(b)$ is the transition probability for the transition $i \to f$. $b(\vartheta)$ is the classical deflection function and $d^2\sigma/d^2\omega|_{el}$ is the elastic cross section calculated for the spherical symmetric potential. This factorization of the inelastic cross section has been examined in the past[36] and appears to be a good approximation for small transition probabilities and small angle scattering.[37]

(2) The transition probability $P(b)$ is calculated using the Born approximation assuming a straight line trajectory. Since the details have been presented elsewhere,[7] we summarize the result for an anisotropic potential term of the type

$$V_n = \frac{A_n}{R^n}\, f(\gamma, \varphi, \dots)\,, \tag{37}$$

where A_n contains the molecular parameters specifying the strength of the interaction with radial dependence R^{-n} and $f(\gamma, \varphi, \dots)$ contains the dependence of the interaction on the angles between the molecular axis or axes and the vector along the internuclear distance. For example for a dipole–dipole electrostatic interaction $n = 3$ and $A_n = \mu_a \mu_b$ (μ is the dipole moment); while for a dipole–quadrupole electrostatic interaction $n = 4$, $A_n = \mu_a Q_b$ (Q is the quadrupole moment), and for an induced dipole–quadrupole induction interaction $n = 7$, $A_n = \alpha_b \mu_a Q_b$ (α is the target dipole–polarizability) etc. The result for $P(b)$ is then[7]

$$P^{i\to f}(b) = a_n^{i\to f}\left(\frac{A_n}{\hbar g b^{n-1}}\right)^2 \sum_{J_b K_b} f_{J_b K_b}(T)\, \frac{|\langle J_b K_b || C(l_b) || J_b' K_b'\rangle|^2}{2J_b + 1} \tag{38}$$

where $a_n^{i\to f}$ is a constant, which depends on the potential term, and the matrix elements of the CsF transition, and $f_{J_b K_b}(T)$ is the fraction of the target molecules in the rotational states J_b and K_b (K is the projection of J on the symmetry axis, important in the case of symmetric tops) and $|\langle \ ||C(l)|| \ \rangle|$ is the Wigner–Eckart matrix element[38] and $C(l)$ describes the multipole moment in the target molecule. For interactions with the quadrupole moment $l = 2$ and $J_b = J_b'$ then[39]

$$\lim_{J_b \to \infty} \frac{\langle J_b || C(2) || J_b'\rangle^2}{2J_b + 1} = \frac{1}{4} \tag{39}$$

and is nearly independent of J_b even for small J_b. However, for symmetric top molecules interacting via their dipole moments, we get for $J_b' = J_b$[39]

$$\frac{|\langle J_b K_b || C(1) || J_b' K_b'\rangle|^2}{2J_b + 1} = \frac{K_b^2}{J_b(J_b + 1)} \tag{40}$$

This result is not unexpected. In the theory of microwave transitions, Eq. (40) corresponds to the square of the transition matrix element of a symmetric top for $J_b' = J_b$ and $K_b' = K_b$.[40]

(3) The classical deflection function $b(\vartheta)$ is approximated by using the classical small angle approximation[41] for a $-C_s/R^s$ potential

$$\vartheta = (s - 1)f(s)\left(\frac{C_s}{E}\right)\frac{1}{b^s}\,, \tag{41}$$

where $f(s) = \sqrt{\pi}/(2)\Gamma[\tfrac{1}{2}(s-1)]/\Gamma(\tfrac{1}{2}s)$. This approximation is valid down to an angle corresponding to the critical laboratory angle given by[42]

$$\Theta_0 \gtrsim \frac{\hbar}{2m_1 v_1}\left(\frac{\pi}{\sigma}\right)^{1/2}$$

which for CsF ($v_1 = 550$ m/s and $\sigma = 10^3$ Å^2) amounts to 2×10^{-4} rad ($\approx 10^{-2\circ}$). Θ_c is thus much smaller than the range of angles of interest here.

(4) The elastic cross section is calculated using a classical small angle formula for a $-C_s/R^s$ potential[41]

$$\frac{d^2\sigma}{d^2\omega}\Big|_{el} = \frac{1}{s}\left(\frac{(s-1)f(s)C_s}{E}\right)^{2/s}\vartheta^{-(2s+2)/s}\,. \tag{42}$$

The validity of this formula has been examined by comparison with semiclassical theory and found to be valid at angles larger than ϑ_c, the center of mass angle corresponding to Θ_c.[41,43]

Inserting Eq. (38), (41) and (42) into Eq. (36), we obtain

$$\frac{d^2\sigma^{i\to f}}{d^2\omega} = \frac{a_n^{i\to f}}{s}\left(\frac{A_n}{\hbar g}\right)^2 \sum_{J_b K_b} f_{J_b K_b}(T)\, \frac{|\langle J_b K_b || C(l) || J_b' K_b'\rangle|^2}{2J_b + 1}$$
$$\times \left((s-1)f(s)\,\frac{C_s}{E}\right)^{4/s - 2n/s}\vartheta^{-(2 + 4/s - 2n/s)} \tag{43a}$$

$$= \sigma_0^{i\to f}\vartheta_0^{-\eta}\left(\frac{\vartheta}{\vartheta_0}\right)^{-\eta} \quad \text{with} \quad \eta = 2 + 4/s - 2n/s\,, \tag{43b}$$

where ϑ_0 is some small center of mass angle in the range probed by the experiment. The choice of ϑ_0 is arbitrary and for convenience we choose $\vartheta_0 = 10^{-2}$ rad. $\sigma_0^{i\to f}\vartheta_0^{-\eta}$ is the differential cross section at $\vartheta = \vartheta_0$. The quantity $\sigma_0^{i\to f}$ is of special interest since it contains all the information on the strength of the inelastic coupling. As seen from Eqs. (43a) and (43b) $\sigma_0^{i\to f}$ is directly proportional to the square of the anisotropic strength parameter A_n. It is also weakly dependent on the spherically symmetric potential parameter C_s in this approximation.

At this point a brief comment on the validity of this simple first order theory is appropriate. Although Eq. (38) gives transition probabilities greater than 1 for small b (violation of unitarity) we may still expect that a simple power-law dependence on the scattering angle Eq. (43b) provides a reasonable approximation of the angular dependence of $d^2\sigma^{i\to f}/d^2\omega$ in the range of interest. In other words this is the simplest realistic approximation one can think of. To be sure if unitarity does break down, $\sigma_0^{i\to f}$ will no longer depend on the square of A_n, but will be a weaker function of A_n. Since the apparatus transmission function preferentially weights the small

TABLE IV. Molecular properties used in correlating the measured cross sections to the interaction potential.

Molecule	α [Å^3][a]	μ [D]	Q [10^{-26} esu cm^2][e]
CsF	3.81	7.89[b]	-20[b]
He	0.21	0	0
Ne	0.41	0	0
Ar	1.64	0	0
Kr	2.48	0	0
Xe	4.02	0	0
CH$_4$	2.56	0	0
CF$_4$	2.82	0	0
SF$_6$	4.48	0	0
C$_2$H$_6$	4.39	0	$\cdots$ 0.60[f]
N$_2$	1.74	0	$\cdots$ 1.5[f] (-1.4[b])
CO	1.94	0.13[b]	$\cdots$ 2.5[f]
CO$_2$	2.59	0	$\cdots$ 4.3[b]
N$_2$O	2.92	0.17[b]	$\cdots$ 3.7[b] (-3.0[f])
CH$_3$Cl	$\cdots$	1.87[c]	$\cdots$
CH$_3$Br	$\cdots$	1.80[c]	$\cdots$
CF$_3$H	$\cdots$	1.65[c]	$\cdots$
CF$_3$Cl	$\cdots$	0.50[c]	$\cdots$
CF$_3$Br	$\cdots$	0.65[d]	$\cdots$

[a]Taken from the tabulation of E. W. Rothe and R. B. Bernstein, J. Chem. Phys. **31**, 1619 (1959).

[b]A. D. Buckingham in Physical Chemistry, Vol. IV, Molecular Properties, edited by D. Henderson (Academic, New York, 1970).

[c]W. Gordy and R. L. Cook, *Microwave Molecular Spectra* (Interscience, New York, 1970).

[d]*Handbook of Chemistry and Physics* 51 Ed. edited by R. C. Weast (The Chemical Rubber Co. Cleveland, 1970).

[e]Where two values are listed, the first was used in the calculations.

[f]A. D. Buckingham, Adv. Chem. Phys. **12**, 107 (1967).

angle region, we may expect this crude approximation to provide a fairly reliable description even though the theory is expected to break down at the larger angles.

In order to determine $\sigma_0 \vartheta_0^{-\eta}$ and σ_0 from the experimental cross sections, Eq. (43b) is inserted into Eq. (31) and integrated over the approximate transmission function Eq. (34). This analysis was carried out for the $(2, 0) \rightarrow (3, 0)$ transition for all the systems listed in Table II. The results for various assumed values of n and s and resulting values of η are listed in Table III. A justification for the choice of n and s will be presented in the discussion of the different major groups below. Examination of the differential cross section $\sigma_0 \vartheta_0^{-\eta}$ at the reference angle ϑ_0 shows clearly the expected increasing trend in progressing from the weak $\alpha \mu Q$ induction potential to the strong μQ and stronger $\mu \mu$-electrostatic potentials. In each case the cross section rises roughly by an order of magnitude. On the other hand the cross section parameter σ_0^{i-f} is nearly the same for all the systems. This rather surprising result arises from the different angular dependence of the cross sections and the differences in the exponent of the spherical interaction term. Thus despite the very approximate nature of the Born approximation the results seem quite reasonable. Next we examine how well the

parameter σ_0^{i-f} correlates with the molecular properties as predicted by Eq. (43a).

A. $\alpha \mu Q$ induction potential

This term has been shown previously to be the predominant anisotropic term of odd parity $[P_1(\cos\gamma)]$ and $[P_3(\cos\gamma)]$ in the long range potential.[7,8] In this case we expect from Eq. (43a) that the following proportionality will hold

$$\sigma_0 \propto \mu_{\text{red}} E_{\text{cm}}^{2/3} C_6^{-5/3} (\alpha_b \mu_a Q_a)^2 \ , \qquad (44)$$

where μ_{red} is the reduced mass and C_6 the coefficient of the R^{-6} long range spherically symmetric potential. Both the spherically symmetric part of the induction potential $(\alpha_b \mu_a^2)$ and the dispersion potential contribute to C_6. For the rare gases the following empirical values were taken from Ref. 44: He, 17.5; Ne, 32.5; Ar, 137.0; Kr, 202.0, and Xe, 319. eV Å^6. Since the necessary data was not available for the spherical molecular targets, their dispersion coefficients were simply estimated from the London formula $C_{6\text{disp}} = \frac{3}{2} \alpha_a \alpha_b I_a I_b (I_a + I_b)^{-1}$ with $\alpha_{\text{CsF}} = 3.81$ Å^3 and $I_{\text{CsF}} = 10.6_\bullet$v . Since it is well known that the London formula yields values which are too small by about a factor 2,[45] the values were all corrected by simply doubling them to yield for C_6: CH$_4$, 270; CF$_4$, 313, and SF$_6$, 500 eV Å^6. This procedure was checked by comparing the estimates for C_6 for the rare gases with the more reliable empirical values and agreement to better than 19% was found. The other molecular parameters are summarized in Table IV. Figure 9 shows a plot of σ_0 for the $(2, 0) \rightarrow (3, 0)$ transition vs $\mu_{\text{red}} \times E_{\text{cm}}^{2/3} C_6^{-5/3} \alpha^2$. With the exception of CF$_4$ and SF$_6$ all the points lie on a straight line within the experimental errors. At least for the remaining partners this strongly suggests that the $\alpha \mu Q$ potential is dominant. The discrepancy in the case of CF$_4$ and SF$_6$ may be due to nuclear contributions to the polarizability from the field induced distortion of the molecules. This effect has been found to be important in ion–molecule scattering experiments.[46] Its contribution is negligible in CH$_4$ but amounts to 36% in CF$_4$ and 46% in SF$_6$.[46] We expect the nuclear polarizability to contribute directly to Eq. (44) as well as to the induction part of C_6 and the resulting effect will shift the points for CF$_4$ in the right direction and bring them closer to the straight line whereas those for SF$_6$ will then lie directly on the straight line. Thus this interpretation provides new evidence for the importance of the nuclear distortion polarizability in collisions where strong electric fields are expected, which in this case are produced by highly polar molecules.

B. Dipole–quadrupole potential

For the linear molecular targets we expect the classical interaction between the dipole moment of the nearly stationary CsF molecule and the quadrupole moment of the target to be the dominant potential. Very little is known about the extent to which this potential is significant in molecular collisions. The first experimental evidence for the importance of this potential was probably provided by our earlier experiments.[7] More recently Dehmer and Wharton[47] and others[48] also observed an enhancement of absolute total cross sections which

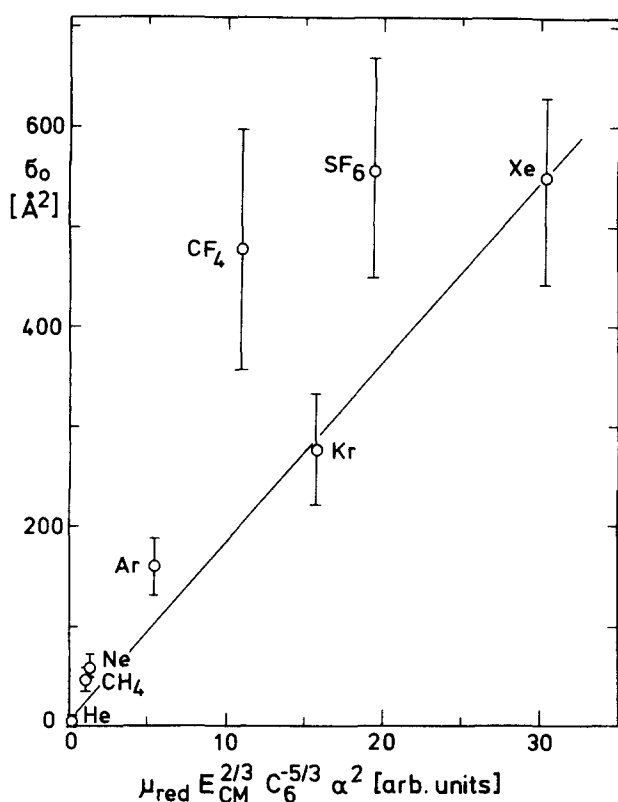FIG. 9. The measured inelastic differential cross section parameters σ_0 for the $(2,0) \to (3,0)$ transition in scattering from the rare gases and spherical molecules are plotted against the quantity $\mu_{\text{red}} \, E_{\text{cm}}^{2/3} \, C_6^{-5/3} \alpha^2$. The linear correlation within the experimental errors indicates that the $\alpha\mu Q$-induction potential is producing the observed transitions.

they attributed to the dipole–quadrupole terms. In neither case however was it possible to establish an entirely satisfactory quantitative agreement between experiment and theory. Indirect evidence for the dipole–quadrupole potential also comes from microwave self-broadening line widths in linear molecules.[49]

Since the expectation value of the quadrupole moment is nonvanishing, we also expect this term to account for the deflection and therefore we set $C_s = \text{const } \mu Q$. With this assumption we expect the following proportionality to hold

$$\sigma_0 \propto \mu_{\text{red}} \, (\mu_a Q_b) \ . \tag{45}$$

Figure 10 shows a plot of σ_0 vs $\mu_{\text{red}} \, Q$ and once more we find a very good correlation. The moleculer properties were taken from Table IV. An attempt was also made to correlate the cross section by assuming that the deflection was due to the long range dispersion forces, but the agreement was not as good as that found in Fig. 10. The good correlation suggests that the Born approximation may be a good approximation. The validity of the correlation and the inversion of the data is beautifully confirmed for the two equal mass pairs N_2 and CO and N_2O and CO_2. In each case the differences in the measured strength parameters correlate nicely with the differences in the quadrupole moments. This result indicates that the small dipole moments of CO and N_2O have a negligible effect on the strength parameter.[49]

The good correlation found in Fig. 10 suggests that the measurement of inelastic cross sections provides a new sensitive method for measuring quadrupole moments. This method has a similar physical basis as the well known method of broadening of microwave spectral lines, but would appear to be more direct and therefore more accurate.

C. Dipole–dipole potential

Very little is known about the differential cross section for collisions in which the dipole–dipole forces predominate. The only previous inelastic scattering experiments are those reported in the earlier paper.[7] In addition there are a number of experiments in which total differential[50] and total integral cross sections[48,51] have been measured. These experiments have recently been surveyed and analyzed in terms of a semiclassical model by Gislason and Herschbach.[52] Unfortunately their results are not directly applicable here since they did not consider state-to-state transitions under conditions similar to those of our experiments.

This rather desolate situation provides a justification for the application of the simple first-order Born approximation even though we expect it to be least valid here. To apply it, we have assumed as in the previous case that the dipole–dipole potential produces both the transitions as well as the deflection. The latter assumption is justified by the results of Gislason and Herschbach who show that the total differential cross section
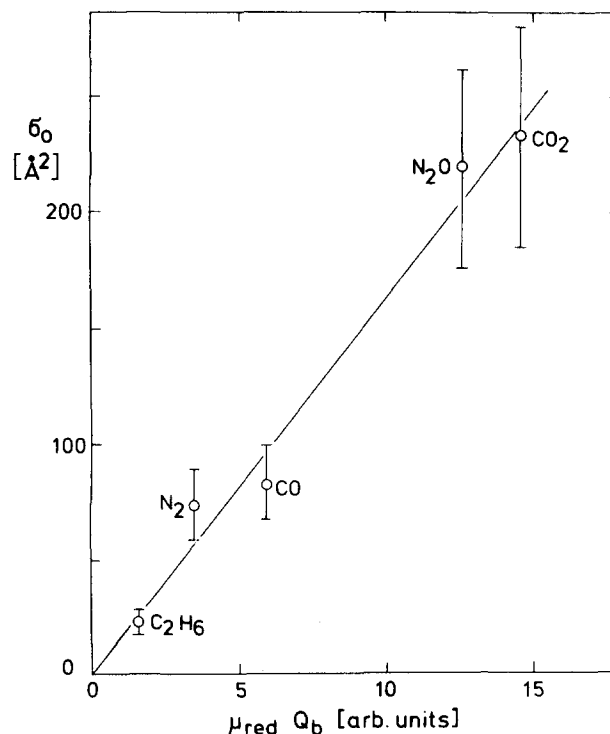

FIG. 10. The inelastic differential cross section parameter σ_0 for the $(2,0) \to (3,0)$ transition in scattering from molecules with large quadrupole moments is plotted against $\mu_{\text{red}} \, Q$. The linear correlation found, indicates that the electrostatic dipole–quadrupole interaction is producing the inelastic transitions and the deflection.
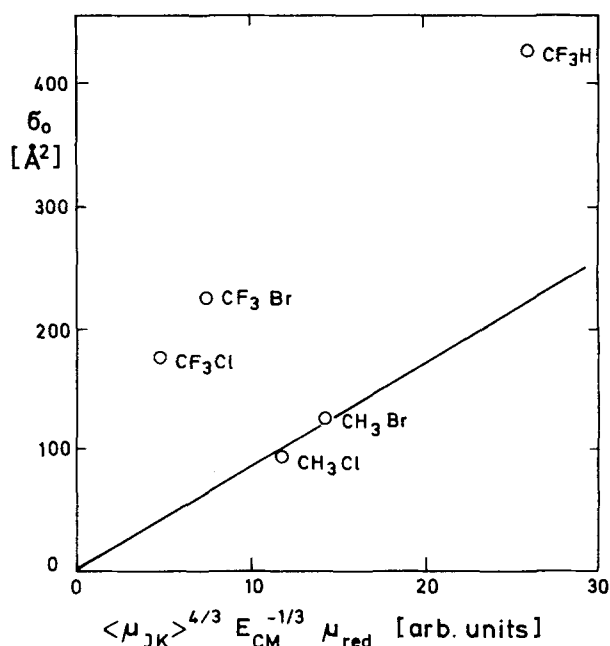
FIG. 11. The inelastic differential cross section parameter σ_0 for the $(2, 0) \rightarrow (3, 0)$ transition in scattering from polar target molecules is plotted against $\langle \mu_{JK} \rangle^{4/3} E_{cm}^{-1/3} \mu_{red}$. The straight line-curve, passing through the ordinate and the points for CH_3Cl and CH_3Br, shows the correlation for molcular targets, where resonance-effects are not expected to be important. The deviations towards larger σ_0 values for CF_3H, CF_3Cl, and CF_3Br are attributed to a resonance contribution, expected for these systems.

for two *nonrotating* dipoles is given by an expression which is directly proportional to Eq. (42) if we set $C_s = \mu_a \mu_b$.

To calculate an expression proportional to σ_0 we must take into account the Wigner–Eckart matrix elements in Eq. (43a). As a result of the thermal weighting factors f_{JK} and the relative importance of states with large K [see Eq. (40)] we expect the effective dipole moments to depend quite significantly on the structure of the symmetric top molecule. Initial evidence for this structural dependence comes from our earlier study[7] where it was found that NH_3 produced a much larger inelastic cross section than the asymmetric top H_2O even though the dipole moment for H_2O is larger than that of NH_3. In the present experiments we are in a position to study this dependence in more detail. CF_3H is an oblate ("pancake") top like NH_3 (neglecting inversion) while the other molecules CH_3Cl, CH_3Br, CF_3Cl, CF_3Br are prolate ("cigar") tops.

For correlating the results it is convenient to introduce $\langle \mu_{JK}^2 \rangle / \mu_0^2$ defined by

$$\frac{\langle \mu_{JK}^2 \rangle}{\mu_0^2} = \sum_{JK} f_{JK}(T) \frac{K^2}{J(J+1)} \quad , \tag{46}$$

where $f_{JK}(T)$ was taken from Townes and Schawlow.[40] Table V summarizes the results. For CH_3Cl and CH_3Br the results could be compared with Birnbaum[53] and reasonable agreement was obtained. Since we do not know the rotational temperature in the target nozzle

beam, we have carried out the calculations for $T_{rot} = 300$, 30, and 10 K. Fortunately the effective dipole moment is only weakly dependent on T_{rot}.

By assuming $\langle \mu_{JK} \rangle \simeq \sqrt{\langle \mu_{JK}^2 \rangle}$ we obtain the following expression for the dependence of σ_0 on the target and collision parameters

$$\sigma_0 \propto \langle \mu_{JK} \rangle^{4/3} E_{cm}^{-1/3} \mu_{red} \quad . \tag{47}$$

The results are shown in Fig. 11. We note that the results do not lie on a common straight line. To explain these deviations we must take into account the possibility of a resonant dipole–dipole interaction, which is not included in our simple treatment. The possibility of resonant dipole–dipole interactions in molecular scattering was pointed out simultaneously by Toennies[7] and Cross and Gordon.[54] Cross and Gordon applied a semi-classical time-dependent theory previously used by van Kranendonck[55] to obtain a resonance function describing the dependence of the total cross section on a rotational matching parameter x, defined by

$$x = \omega b / v \tag{48}$$

where $\omega = \Delta E_1 + \Delta E_2 / \hbar$ and ΔE_1 and ΔE_2 are the energy changes occurring in the two molecules. For small x ($x \lesssim 1$) the cross section is largest and for $x \simeq 2$ it is expected to drop off by a factor of about 2. Examination of Table V shows that the CF_3X molecules all have rotational constants quite close to that of CsF ($B_{rot} = 5.527 \times 10^3$ MHz). Thus for these molecules we expect an additional enhancement of the cross sections due to resonant transitions. The explicit quantitative treatment of these processes requires a detailed knowledge of the rotational state distribution in the nozzle beams of these symmetric molecules. Since we do expect extensive rotational cooling, a large proportion of the molecules will be in low-lying states for which resonance is possible. For this reason we have drawn a straight line through the cross sections for CH_3Cl and CH_3Br for which the frequencies are too large for resonance to be possible. We attribute the increase in the cross sections over this straight line found for the CF_3X systems to the resonant contribution. On the basis of this simple picture the CF_3Cl and CF_3Br cross sections are enhanced by a factor between 3 and 4, whereas the CF_3H cross section is only about a factor 2 larger because of the resonance process. This difference is quite rea-

TABLE V. Rotational constants and calculated thermally expectation values of the dipole moment of symmetric top molecules for three different temperatures.

		Rotational constants 10^3 MHz			$\frac{\langle \mu_{JK}^2 \rangle}{\mu_0^2}$		
		A	B	C	$T = 300$ K	$T = 30$ K	$T = 10$ K
CH_3Cl	prolate	150	13.29	$\cdots$	0.0946	0.145	0.178
CH_3Br	prolate	148	9.53	$\cdots$	0.077	0.118	0.146
CF_3H	oblate	$\cdots$	10.35	5.67	0.416	0.451	0.475
CF_3Cl	slightly prolate	5.76	3.34	$\cdots$	0.263	0.287	0.306
CF_3Br	slightly prolate	5.74	2.10	$\cdots$	0.211	0.230	0.246

sonable since on the basis of the rotational frequencies in Table V we would expect the former molecules to have more states which could be in resonance at any one given temperature.

In summary then our simple model, when modified to take into account resonant processes, also appears to provide a reasonable description of dipole–dipole interactions.

VIII. CONCLUSIONS

It has been possible to measure incomplete integral inelastic cross sections for up to five different transitions between low-lying j, m states for 18 different scattering partners. In addition to pure Δj transitions ($\Delta m = 0$), the observed transitions also include Δm transitions with and without changes in j. As far as we are aware, this is the first observation of Δm transitions in a scattering experiment. The experimental arrangement allows for the first time a complete specification of all the parameters which define the inelastic cross sections. The velocities of both beams are narrowly distributed and known. The molecules are polarized and oriented by an electric field perpendicular to the collision direction. Becasue of these nearly ideal conditions the transmission function, which gives the contributions from the various center of mass angles accepted by the apparatus, has been calculated and can be used to analyze the data in terms of differential cross sections in the center of mass systems. Such an analysis has been carried out and it is shown that, depending on the multipole moments and structure of the target molecules, different terms in the classical induction or electrostatic potential dominate the interaction. These results show that the inelastic cross sections are extremely sensitive to the anisotropic terms in the potential. Much additional work is however needed before these results are fully understood.

ACKNOWLEDGMENTS

[1]For a recent review see J. P. Toennies, Ann. Rev. Phys. Chem. 27, 225 (1976).

[2]M. Faubel and J. P. Toennies, Adv. Atomic and Mol. Phys. 13, 229 (1977).

[3](a) H. G. Bennewitz, K. Kramer, W. Paul, and J. P. Toennies, Z. Phys. 177, 84 (1964); (b) For a recent review of beam experiments with state selectors see J. Reuss, Adv. Chem. Phys. 30, 389 (1976); and (c) For recent papers using laser methods see M. P. Sinha, C. D. Caldwell, and R. N. Zare, ibid. 61, 491 (1974) and A. G. Visser, J. P. Bekooy, L. K. Van der Meij, C. De Vrengd, and J. Korving, Chem. Phys. 20, 391 (1977).

[4](a) H. Van den Bergh, M. Faubel, and J. P. Toennies, Fara-

day Discuss. 55, 203 (1973); (b) K. Rudolph and J. P. Toennies, J. Chem. Phys. 65, 4483 (1976); (c) W. R. Gentry and C. F. Giese, J. Chem. Phys. 67, 5389 (1977); and (d) U. Buck, F. Huisken, J. Schleussener, and H. Pauly, Phys. Rev. Lett. 38, 680 (1977).

[5](a) See for example, H. J. Loesch, Chem. Phys. 18, 431 (1976); (b) For an up to date list of systems studied see Ref. 2.

[6](a) J. P. Toennies, Disc. Faraday Soc. 33, 96 (1962); (b) J. P. Toennies, Z. Phys. 182, 257 (1965).

[7]J. P. Toennies, Z. Phys. 193, 76 (1966).

[8]U. Borkenhagen, H. Malthan, and J. P. Toennies, Chem. Phys. Lett. 41, 222 (1976).

[9]J. M. Henrichs, R. P. M. de Bie, C. G. H. Simons, and N. F. Verster (to be published); J. M. Henrichs, Ph.D. thesis (Technische Hogeschool, Eindhoven, 1979).

[10]This paper is based largely on the Ph.D. thesis of H. Malthan and U. Borkenhagen. These theses are available: (a) H. Malthan, Max-Planck-Institut für Strömungsforschung, Bericht 16/1976 and (b) U. Borkenhagen, Max-Planck-Institut für Strömungsforschung, Bericht 1/1977.

[11]For additional experimental details see Ref. 10. An unabridged version of this paper (in English) also contains additional information: U. Borkenhagen, H. Malthan, and J. P. Toennies, Max-Planck-Institut für Strömungsforschung, Bericht (1979).

[12]Xenon was used since its mass is the closest to that of CsF. With xenon and the other rare gases Kr and Ar no significant velocity slip was found and the CsF always had the same terminal velocity as estimated for the rare gas. However, for obtaining the best focussing in the electrostatic quadrupole, a low velocity is desirable and Xe was used for this reason. For more details on the mixed gas beam properties see Ref. 10a and 14.

[13](a) H. G. Bennewitz and G. Buess, Chem. Phys. 28, 175 (1978); See also (b) P. K. Sharma, W. S. Young, W. E. Rodgers, and E. L. Knuth, J. Chem. Phys. 62, 341 (1975).

[14](a) H. Malthan and J. P. Toennies, Prox. IXth Int. Symp. Rarefied Gas Dynamics, Göttingen II, 14 (1974); (b) U. Borkenhagen, H. Malthan, and J. P. Toennies, J. Chem. Phys. 63, 3173 (1975).

[15]See for example, R. Kaiser and G. Gottschalk, Elementare Tests zur Beurteilung von Meßdaten (BI Hochschultaschenbücher 774, 1972).

[16]See for example, S. Brandt, Statistische Methoden der Datenanalyse (BI Hochschultaschenbuch 816/816a, 1968).

[17]H. G. Bennewitz and H. D. Dohmann, Vakuum-Technik 14, 8 (1965).

[18]J. B. Anderson, in Molecular Beams and Low Density Gasdynamics, edited by P. P. Wegener (Dekker, New York, 1974).

[19]G. Brusdeylins, unpublished.

[20]The effective scattering paths for He and Ne were not checked in this way since the second method would have required large cross section corrections resulting from the limited angular resolving power in the center of mass system for these light systems.

[21]I. E. Dayton, F. C. Shoemaker, and R. F. Mozley, Rev. Sci. Instrum. 25, 485 (1954).

[22]J. J. Everdij, A. Huyser, N. F. Verster, Rev. Sci. Instrum. 44, 721 (1973).

[23]L. Wharton, M. Kaufmann, and W. Klemperer, J. Chem. Phys. 37, 621 (1962). The formula (7) is incorrect and should read

$$A = \frac{(J^2 - M^2)\,(J-1)^2 - M^2}{8J^2\,(2J-3)\,(2J-1)^3\,(2J+1)}\ .$$

[24]J. H. Shirley, J. Chem. Phys. 38, 2896 (1963).

[25]J. E. Mosch, Max-Planck-Institut für Strömungsforschung, Report No. 117/72, Göttingen 1972.

[26]R. P. M. de Bie, Afstudeerwerk No. 77-04, Technische Hogeschool Eindhoven, Afdeling der Technische Naturkunde.

[27]See AIP document no. PAPS JCPSA-71-1722-11 for 10 pages of calculated transmission functions defined by Eq. (31) and (32) for the rare gases He, Ne, Ar, Kr, and Xe for most of the transitions in Table II. Order by PAPS number and journal reference from American Institute of Physics, Physics Auxiliary Publication Service, 335 East 45th Street, New York, N.Y. 10017. The price is $1.50 for each microfiche (98 pages), or $5 for photocopies of up to 30 pages with $0.15 for each additional page over 30 pages. Airmail additional. Make checks payable to the American Institute of Physics. This material also appears in Current Physics Microform, the monthly microfilm edition of the complete set of journals published by AIP, on the frames immediately following this journal article.

[28]A. D. Buckingham, Adv. Chem. Phys. 12, 107 (1967).

[29]For calculations for TlF—Ar and CsF—Ar and related systems using the sudden or high energy calculations see for example Ref. 7 and (a) K. H. Kramer and R. B. Bernstein, J. Chem. Phys. 40, 200 (1964); 44, 4473 (1966), and R. W. Fenstermaker, J. Chem. Phys. 47, 4417 (1967); (b) S. Saha and E. Guha, J. Phys. B 8, 2293 (1975), S. S. Bhattacharyya, S. Saha, and A. K. Barua, J. Phys. B 11, 1965 (1978). Calculations based on the exponential Born approximation have been reported by (c) S. Bosanac and G. G. Balint-Kurti, Mol. Phys. 29, 623 (1975); and (d) D. E. Fitz and P. McGuire, Chem. Phys. Lett. 44, 503 (1976); D. E. Fitz, Chem. Phys. 24, 133 (1977).

[30]For TlF—Ar and CsF—Ar and related systems using the IOS approximation see T. P. Tsien, G. A. Parker, and R. T Pack, J. Chem. Phys. 59, 5373 (1973), Ref. 29d and Ref. 31.

[31]A. S. Dickinson and D. Richards, J. Phys. B At. Mol. Phys. 11, 1085 (1978).

[32]U. Borkenhagen, G. Meyer, and J. P. Toennies (to be published).

[33]J. van de Ree, J. Chem. Phys. 54, 3249 (1971).

[34]J. P. Toennies, W. Welz, and G. Wolf, J. Chem. Phys. 61, 2461 (1974); 64, 5305 (1976); and (to be published).

[35]Well depths ε have been measured for CsF on He and Ar H. G. Bennewitz, R. Haerten, and G. Müller, Z. Phys. 226, 139 (1969) and Kr and Xe, R. David, W. Spoden, and J. P. Toennies, J. Phys. B 6, 897 (1973). These reported values are probable much too small as pointed out by W. D. Armstrong, R. J. Conley, R. P. Creaser, E. F. Greene,

and R. B. Hall, J. Chem. Phys. 63, 3349 (1975), and K. A. Reed, and L. Wharton, J. Chem. Phys. 66, 3399 (1977). At the moment it appears as if ε is not even roughly known for these systems.

[36]W. H. Miller, J. Chem. Phys. 49, 2373 (1968).

[37]We have compared the results of calculations using the exponential sudden approximation in which this assumption is made with the results of an infinite order sudden (IOS) approximation and get agreement to within about 20%. We thank G. Meyer and D. E. Fitz for carrying out the IOS calculations.

[38]A. R. Edmonds, Angular Momentum in Quantum Mechanics (Princeton University, Princeton, New Jersey, 1957).

[39]See Ref. 7, pp. 114–118.

[40]C. H. Townes and A. L. Schawlow, Microwave Spectroscopy (McGraw-Hill, New York, 1955).

[41](a) H. Pauly and J. P. Toennies, Ad. Atom. Mol. Phys. 1, 195 (1965); (b) R. B. Bernstein, Adv. Chem. Phys. x, 75 (1966).

[42]H. Pauly and J. P. Toennies, Meth. Expt. Phys. 7A, 227 (1968).

[43]R. W. Anderson, J. Chem. Phys. 60, 2680 (1974).

[44]U. Borkenhagen, G. Meyer, and J. P. Toennies (to be published).

[45]See Ref. 41a, p. 205.

[46]E. A. Gislason, F. E. Budenholzer, and A. D. Jorgensen, Chem. Phys. Lett. 47, 434 (1977).

[47]P. M. Dehmer and L. Wharton, J. Chem. Phys. 61, 4209 (1974).

[48]R. J. Cross Jr., E. A. Gislason, and D. R. Herschbach, J. Chem. Phys. 45, 3582 (1966).

[49]W. S. Benedict and R. Herman, J. Quant. Spectrosc. Radiat. Trans. 3, 265 (1963).

[50](a) R. Helbing and H. Pauly, Z. Phys. 179, 16 (1964); (b) R. W. Bickes, G. O. Este, G. Scoles, and K. M. Smith, J. Phys. B 7, L19 (1974).

[51]J. T. Cheung, J. Chem. Phys. 64, 5317 (1976).

[52]E. A. Gislason and D. R. Herschbach, J. Chem. Phys. 24, 2133 (1976).

[53]G. Birnbaum, J. Chem. Phys. 27, 360 (1957).

[54]R. J. Cross Jr. and R. G. Gordon, J. Chem. Phys. 45, 3571 (1966).

[55]J. Van Kranendonk, Can. J. Phys. 41, 433 (1963).